Available online at www.sciencedirect.com

SciVerse ScienceDirect

Geochimica et Cosmochimica Acta 93 (2012) 77–101

Geochimica et Cosmochimica Acta

www.elsevier.com/locate/gca

Circumstellar and interstellar material in the CO3 chondrite ALHA77307: An isotopic and elemental investigation

Maitrayee Bose [a], Christine Floss [a,*], Frank J. Stadermann [a], Rhonda M. Stroud [b], Angela K. Speck [c]

[a] *Laboratory for Space Sciences and Physics Department, Washington University, St. Louis, MO 63130, USA*
[b] *Naval Research Laboratory, Washington, DC 20375, USA*
[c] *University of Missouri, Columbia, MO 65211, USA*

Received 7 October 2011; accepted in revised form 23 June 2012

Abstract

We have carried out a NanoSIMS C, N and O ion imaging study of the CO3.0 chondrite ALHA77307. The distribution of O-anomalous grains in ALHA77307 is similar to that observed in other primitive meteorites, and is dominated (84%) by ^{17}O-rich Group 1 grains from low-mass asymptotic giant branch (AGB) stars of close-to-solar metallicity. Four percent of the grains belong to Group 2, whose ^{18}O depletions suggest cool-bottom processing in low-mass stars during the AGB phase, while 8% are Group 4 grains with likely origins in Type II supernova (SN) ejecta. One ferromagnesian silicate has a very high ^{17}O enrichment; nova explosions have been suggested as sources for such grains, but recent models with updated reaction rates show large discrepancies with the grain data, leaving the origins of these grains uncertain.

Most of the grains are silicates (86%) with the remainder consisting of oxides (8%), three silica grains and two 'composite' grains composed of multiple subgrains with different elemental compositions. The elemental compositions of the silicates are similar to those found in other studies, with a predominance of non-stoichiometric compositions and high (up to 44 at.%) Fe concentrations. A comparison of isotopic and elemental compositions for all presolar silicates shows that olivine compositions are overabundant in Group 4 grains compared to grains from Groups 1 and 2. This may reflect injection of presolar material from a nearby supernova into the early solar nebula and incorporation into parent bodies before alteration of compositions through irradiation and sputtering in the interstellar medium, as is likely to have occurred for the Group 1 and 2 grains from more distant AGB stars.

The matrix material in ALHA77307 contains abundant carbonaceous hotspots with excesses in ^{15}N. However, unlike CR chondrites, the insoluble organic matter (IOM) in ALHA77307 does not have a bulk N isotopic anomaly, consistent with Raman evidence that it has experienced more processing than IOM from CR chondrites. Nevertheless, secondary processing has clearly not been so pervasive as to lead to complete destruction of N isotopic anomalies in this meteorite. Moreover, presolar silicate abundances and elemental compositions show little evidence for thermal processing, indicating a decoupling of the effects of metamorphism on organic matter and matrix silicates.

1. INTRODUCTION

Presolar material includes grains that formed around evolved stars and organic matter that formed in cold molecular clouds. These materials survived the collapse of the molecular cloud from which our solar system originated and are available for investigation in primitive meteorites, comets, interplanetary dust particles (IDPs), and Antarctic micrometeorites. Coordinated analyses using various analytical techniques can provide information about the stellar sources of the grains and allow testing of condensation models. These laboratory studies (e.g., Zinner, 2007) also

* Corresponding author.
E-mail address: floss@wustl.edu (C. Floss).

0016-7037/$ - see front matter © 2012 Elsevier Ltd. All rights reserved.
http://dx.doi.org/10.1016/j.gca.2012.06.027

give us insights into processing in the early solar nebula, in the interstellar medium, and in the parent bodies in which these grains are found.

It is now well established that presolar silicates are the most abundant type of presolar grain, with abundances of ~375 ppm in primitive anhydrous IDPs (Floss et al., 2006) and up to ~200 ppm in largely unaltered carbonaceous chondrites (Nguyen et al., 2007, 2010a; Floss and Stadermann, 2009a; Vollmer et al., 2009a). Ion imaging of matrix material in primitive meteorites has also resulted in the identification of abundant presolar SiC, as well as carbonaceous material with N, and occasionally C, isotopic anomalies (e.g., Busemann et al., 2006; Floss et al., 2006; Floss and Stadermann, 2009b,c).

Allan Hills (ALHA) 77307 is a CO3.0 chondrite (Brearley, 1993) whose fine-grained matrix consists of abundant amorphous dust and unequilibrated assemblages of Fe- and Si-rich material (Scott and Jones, 1990). ALHA77307 has experienced minimal thermal metamorphism and aqueous alteration (e.g., Scott and Jones, 1990; Brearley, 1993; Grossman and Brearley, 2005; Bonal et al., 2007), but Raman analyses indicate that its insoluble organic matter (IOM) is less disordered than that of many CR and ungrouped C chondrites (Busemann et al., 2007), suggesting some thermal processing of the organics. Previous investigations have shown the presence of abundant presolar silicate grains in this meteorite (Nguyen et al., 2010a). In this study we have carried out additional O isotope imaging to obtain a more comprehensive inventory of the presolar grain population in this meteorite and to identify grains with unusual (isotopic and elemental) compositions. We also report the first results of C and N isotopic imaging on ALHA77307 and discuss the implications of the results. Preliminary data were reported by Bose et al. (2009, 2010a,b, 2011a,b).

2. SAMPLES AND EXPERIMENTAL

A polished thin section of ALHA77307 was obtained from the curatorial facility at the Johnson Space Center, Houston. Prior to carrying out NanoSIMS analyses, transmitted- and reflected-light images were taken with an Olympus BH-2 optical microscope. The transmitted-light images allowed identification of the dark fine-grained matrix areas where presolar grains are sited, while the reflected-light images aided sample navigation in the NanoSIMS.

NanoSIMS C, N and O ion imaging was carried out by rastering a Cs^+ primary beam of about 1 pA (~100 nm diameter) over areas of ALHA77307 matrix material and collecting secondary ions ($^{12}C^-$ $^{13}C^-$, $^{16}O^-$, $^{17}O^-$, $^{18}O^-$ or $^{12}C^-$, $^{13}C^-$, $^{12}C^{14}N^-$, $^{12}C^{15}N^-$, $^{28}Si^-$) and secondary electrons (SEs) in multi-collection mode. Prior to acquiring the isotopic data, $12 \times 12\ \mu m^2$ areas in the matrix were sputtered at a higher beam current (~25 pA), in order to locally remove the carbon coating on the thin section and to implant Cs^+ to enhance secondary ion production; the measurements were made in 10×10 μm (256^2 pixels) areas within these presputtered regions. Measurements were done in automated mode, following a predefined grid pattern and each measurement consisted of a series of 5–10 layers that were added together to constitute a single image measurement. This procedure allows for correction of possible image shifts during the measurements and allows isotopic anomalies to be tracked through sequential layers. Carbon and O imaging was also carried out on a FIB section made from one of the grains.

Oxygen-, C- and N-anomalous grains were identified from $^{17}O^-/^{16}O^-$ and $^{18}O^-/^{16}O^-$, $^{12}C^-/^{13}C^-$, and $^{12}C^{14}N^-/^{12}C^{15}N^-$ ratio images, respectively. We define a grain as presolar if any of its isotopic ratios differ from terrestrial values ($^{16}O/^{17}O = 2625$; $^{16}O/^{18}O = 499$; $^{12}C/^{13}C = 89$; $^{14}N/^{15}N = 272$) by 5σ or more, and the isotopic anomaly can be traced through at least three consecutive layers of the measurement. All isotopic ratios are internally normalized, assuming terrestrial isotopic compositions for the bulk matrix. Although some chondrite groups (e.g., the CR chondrites) exhibit anomalous bulk N isotopic compositions, this is not the case for ALHA77307. Nitrogen isotopic anomalies are carried by the IOM of their host meteorites (e.g., Busemann et al., 2006; Alexander et al., 2007) and the bulk IOM of ALHA77307 has a terrestrial N isotopic composition (Alexander et al., 2007). While another N-anomalous component could conceivably be present in the matrix of ALHA77307, this would have evident from large-scale N isotopic variations in our ion images, which were not observed.

Subsequent to the identification of isotopically anomalous phases in the NanoSIMS, elemental compositions were determined using standard procedures developed for the analysis of presolar silicate grains (e.g., Bose et al., 2010c). Multiple Auger spectra are acquired over the grains of interest at a beam current setting of 10 kV and 0.25 nA. The spectra are examined for artifacts and are then added together to constitute a single spectrum for each grain. Secondary electron images are acquired before and after each set of spectral analyses to monitor for image shifts during the measurement. The Auger spectra were often complemented by maps of specific elements of interest (e.g., Ca, O, Fe, Mg, Al, Si). Elemental mapping was carried out at 10 keV and 5 nA, and typically consisted of 3–40 scans over $2 \times 2\ \mu m^2$ or $4 \times 4\ \mu m^2$ areas that contained the grain of interest.

Elemental compositions of the O-anomalous grains were calculated from the Auger spectra using sensitivity factors for O, Si, Fe, Mg, Ca, and Al obtained from olivine and pyroxene standards (Stadermann et al., 2009). The experimentally derived sensitivity factors and the relative uncertainties are O: 0.194 [3.6%], Si: 0.121 [11.0%], Mg: 0.234 [9.4%], Fe: 0.150 [11.2%], Ca: 0.626 [10.8%], and Al: 0.160 [24.9%]. In addition to these analytical uncertainties, the measurements reported in this study may also be affected by other factors, including the presence of residual surface contamination (e.g., O, C) and low signal-to-noise ratios; these non-random effects are difficult to quantify, but can affect the analyses beyond the stated uncertainties. Hematite (Fe_2O_3) and periclase (MgO) standards were measured in order to determine quantitative elemental compositions for several oxide grains. The spectra of a few silicate grains show small S peaks. However, elemental mapping shows that the S is not intrinsic to the grains, but appears

to be due to contamination from the surrounding matrix. This element has, therefore, not been included in quantification of the silicate grain compositions. Quantitative Auger data are not reported for SiC and carbonaceous grains. Instead, Auger spectra and elemental maps were used to qualitatively identify these phases.

One presolar grain, 21420, was investigated with the 200 kV JEOL 2200FS TEM at the Naval Research Laboratory. The sample was extracted by focused ion beam (FIB) lift-out (e.g., Zega et al., 2007) using the FEI Nova NanoLab 600. Energy dispersive X-ray (EDX) analysis was carried out to determine grain chemistry, and selected elements (Al, Ca, Fe, Mg, O, and Si) were mapped over a 0.7×0.7 μm^2 area of the FIB section. Selected-area electron diffraction was carried out, where possible, to identify crystal structures.

3. RESULTS

3.1. Isotopic and elemental compositions of O-anomalous grains

Eighty-eight O-anomalous grains were identified from 17,100 μm^2 of matrix material (Fig. 1; Table 1). Seventy-four grains (84%) have ^{17}O-rich compositions with close-to-solar ^{18}O/^{16}O ratios (Group 1; Nittler et al., 1997). One grain shows an unusually high ^{17}O enrichment with a ^{17}O/^{16}O ratio of $(89.3 \pm 0.6) \times 10^{-4}$ (Fig. 1). Four grains (4%) have larger depletions in ^{18}O/^{16}O ratios than typical Group 1 grains ($<\sim 10^{-3}$) and belong to Group 2. Group 3 (^{16}O-rich) grains are rare and only one such grain was identified in our study. Seven grains (8%) are ^{18}O-rich, some with small ^{17}O anomalies, and belong to Group 4. Our results are in good agreement with the study of Nguyen et al. (2010a), who found similar relative distributions of the grain types (e.g., 87% Group 1; 6% Group 4).

Seventy-eight of the O-anomalous grains were characterized in the Auger Nanoprobe and were classified into

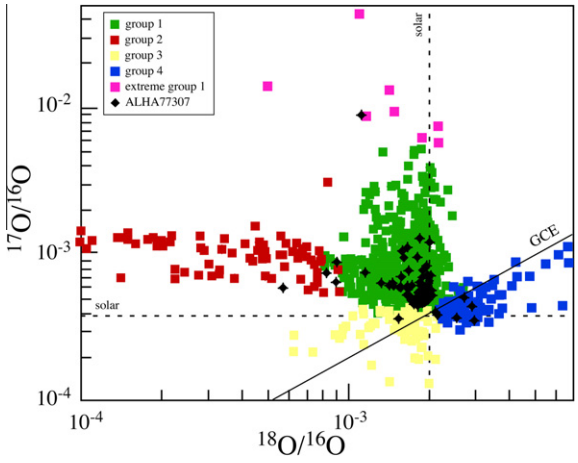

Fig. 1. Oxygen three-isotope plot showing O-anomalous grains from ALHA77307 and the literature (data from the presolar grain database: http://presolar.wustl.edu/~pgd/). GCE: Galactic Chemical Evolution line (see text). Errors are 1σ.

67 silicate, six oxide (one Mg-oxide, three Al-oxide and two Fe-oxide), three SiO_2 and two composite grains (Table 2). The remaining ten grains could not be characterized because they were sputtered away during the NanoSIMS measurements. The abundances of presolar silicates and oxides identified in this study are 119 ± 14 ppm and 22 ± 9 ppm (errors are based only on counting statistics). Detailed descriptions of the grains follow.

3.1.1. Mg-oxide

Grain 55b-4 (Group 1) is a near-spherical grain that is about 420 nm in diameter. The Auger spectrum shows the presence of Mg and O peaks, and the absence of any other elements (Fig. 2). Comparison of the grain composition to a periclase (MgO) standard indicates a Mg/O ratio of 1.0 ± 0.1 (i.e., MgO); this is the first report of a presolar grain with this composition.

3.1.2. SiO_2

Three Group 1 grains (21420, 2132, and 10-4-bm) exhibit only O and Si in their Auger spectra (Fig. 3), with O/Si ratios of 2.2 ± 0.3, 2.2 ± 0.3, and 1.9 ± 0.2, respectively (Table 2), consistent with SiO_2. Grain 2132 has a diameter of ~220 nm with a poorly defined grain boundary while grain 10-4-bm is the largest of the three with a diameter of ~320 nm. Grain 21420 has a complete grain boundary and is ~300 nm in diameter. We attempted to determine the crystal structure of silica grain 21420 using FIB/TEM. EDX spectra and elemental maps of the extracted section confirmed the presence of a 140 nm wide × 50 nm high Si-rich grain (Fig. 4). High resolution imaging and selected area diffraction indicate that the grain is completely amorphous. SIMS-induced amorphization has been observed previously in FIB-extracted sections of presolar oxide grains (Zega et al., 2011), and we cannot completely rule out the possibility that the grain was originally crystalline. However, we would not expect such a layer to extend more than approximately 10–20 nm below the surface and, thus, it seems likely that this is a primary feature of the grain. We attempted to re-confirm the anomalous oxygen isotopic composition of the grain by NanoSIMS, but the remaining volume was too small to obtain definitive results.

3.1.3. Al-oxides

Grains 31 and 52-4-O (Group 1) and grain 45 (Group 4) are dominated by O and Al (Fig. 5), with Al/O ratios of 0.4, 0.5 and 0.4, respectively (Table 2). These grains are more O-rich than expected for Al_2O_3 (Al/O = 0.67). The elevated O concentration could be an intrinsic feature of the grains, but could also be due to analytical artifacts, such as residual atmospheric contamination on the grain surfaces or inappropriate sensitivity factors. We note, however, that an Al-oxide grain from MET 00426, quantified using the same sensitivity factors, is stoichiometric Al_2O_3 (Floss and Stadermann, 2009a).

3.1.4. Fe-oxides

Grain 21412 (Group 4) and grain 54-7 (Group 1) are both ~165 nm in diameter and show only Fe and O in their

Table 1
O isotopic compositions of presolar silicates and oxides in ALHA77307.

Grain name	$^{18}O/^{16}O$ ($\times 10^{-3}$)	$^{17}O/^{16}O$ ($\times 10^{-4}$)	Group	Size* (nm)
133	0.84 ± 0.01	7.51 ± 0.14	2	560 × 520
5b-7	1.85 ± 0.03	4.48 ± 0.12	1	360 × 320
10-4-tp	1.93 ± 0.05	7.84 ± 0.30	1	320 × 160
11-1-lt	2.05 ± 0.05	12.1 ± 0.4	1	160 × 160
11-1-rt	2.03 ± 0.03	5.46 ± 0.16	1	320 × 280
15-5-bm	1.97 ± 0.03	4.70 ± 0.17	1	250 × 150
18-6	1.97 ± 0.04	4.78 ± 0.17	1	170 × 170
18-7	1.70 ± 0.03	5.81 ± 0.16	1	320 × 240
54-1	1.69 ± 0.03	6.12 ± 0.18	1	130 × 130
48-bm	2.10 ± 0.02	5.27 ± 0.13	1	280 × 160
1310	1.58 ± 0.02	5.96 ± 0.15	1	330 × 230
5b-8	2.19 ± 0.03	3.91 ± 0.11	4	480 × 120
63	2.06 ± 0.03	5.09 ± 0.14	1	320 × 240
8a-4-bm	1.90 ± 0.04	6.15 ± 0.20	1	400 × 320
10-4-O18	2.95 ± 0.04	4.45 ± 0.17	4	280 × 200
114	1.81 ± 0.04	5.01 ± 0.18	1	320 × 120
116	2.06 ± 0.05	7.27 ± 0.29	1	600 × 240
12-4	1.84 ± 0.04	9.64 ± 0.28	1	400 × 240
128	2.19 ± 0.04	3.86 ± 0.15	4	300 × 300
17b-2	1.85 ± 0.04	5.52 ± 0.23	1	280 × 160
51-6-O17	1.93 ± 0.04	5.35 ± 0.18	1	270 × 130
52-15	1.69 ± 0.05	11.2 ± 0.4	1	400 × 400
53-5	1.99 ± 0.04	4.98 ± 0.18	1	230 × 200
53-11	1.91 ± 0.04	4.68 ± 0.17	1	300 × 150
54-9	3.01 ± 0.04	3.55 ± 0.15	4	300 × 240
111-O	0.92 ± 0.01	8.97 ± 0.16	2	100 × 100
112	1.68 ± 0.02	5.32 ± 0.11	1	400 × 320
1-24	2.04 ± 0.03	6.39 ± 0.15	1	320 × 240
132	1.91 ± 0.03	5.02 ± 0.16	1	400 × 200
146	1.57 ± 0.02	3.65 ± 0.11	3	520 × 240
178	2.04 ± 0.04	6.62 ± 0.23	1	160 × 80
2131	1.93 ± 0.02	7.02 ± 0.15	1	370 × 320
21422	1.93 ± 0.03	5.77 ± 0.18	1	240 × 200
2-1425-O2	1.99 ± 0.02	6.19 ± 0.14	1	560 × 320
32	1.72 ± 0.02	5.25 ± 0.16	1	280 × 200
42	1.96 ± 0.02	4.91 ± 0.13	1	320 × 240
44-O	1.61 ± 0.02	7.04 ± 0.18	1	200 × 200
48-tp	2.04 ± 0.03	5.04 ± 0.15	1	360 × 280
410	1.78 ± 0.02	4.63 ± 0.14	1	250 × 230
7d-2	1.74 ± 0.03	4.89 ± 0.17	1	400 × 200
8a-3-O17	1.87 ± 0.03	5.60 ± 0.17	1	280 × 200
107	2.02 ± 0.04	4.87 ± 0.18	1	240 × 120
113	2.01 ± 0.04	7.29 ± 0.22	1	200 × 160
13-4	2.00 ± 0.04	5.91 ± 0.19	1	250 × 150
15-5-tp	1.92 ± 0.04	6.16 ± 0.20	1	200 × 180
51-7	1.76 ± 0.03	4.98 ± 0.14	1	180 × 100
51-9	1.89 ± 0.04	12.8 ± 0.35	1	530 × 250
53-4	2.04 ± 0.04	5.35 ± 0.19	1	160 × 140
131	1.99 ± 0.03	5.81 ± 0.15	1	250 × 180
163	1.13 ± 0.02	89.3 ± 0.6	1x	320 × 200
1710	1.86 ± 0.03	4.91 ± 0.18	1	400 × 240
44-O17	1.99 ± 0.02	5.64 ± 0.15	1	280 × 240
8a-3-O	0.92 ± 0.02	6.55 ± 0.19	2	480 × 200
8a-4-tp	2.02 ± 0.04	5.19 ± 0.17	1	360 × 120
105	1.94 ± 0.04	5.71 ± 0.20	1	160 × 120
121	1.60 ± 0.03	6.06 ± 0.17	1	280 × 200
127	1.60 ± 0.03	5.93 ± 0.17	1	400 × 400
13-5	1.76 ± 0.04	6.15 ± 0.23	1	320 × 280
51-6-O	1.71 ± 0.03	5.19 ± 0.17	1	320 × 150
52-8	1.88 ± 0.04	4.74 ± 0.21	1	200 × 190

(*continued on next page*)

Table 1 *continued*

Grain name	$^{18}O/^{16}O$ ($\times10^{-3}$)	$^{17}O/^{16}O$ ($\times10^{-4}$)	Group	Size* (nm)
53-6	2.02 ± 0.03	5.33 ± 0.16	1	200 × 100
54-5	1.90 ± 0.03	5.30 ± 0.18	1	200 × 120
52-4-O17	1.88 ± 0.03	6.5 ± 0.2	1	160 × 120
10-4-bm	1.61 ± 0.05	10.5 ± 0.36	1	360 × 280
2132	1.93 ± 0.02	5.89 ± 0.12	1	280 × 160
21420	1.99 ± 0.03	8.41 ± 0.18	1	300 × 300
2-1425-O1	2.59 ± 0.03	3.69 ± 0.11	4	380 × 200
19-1	1.35 ± 0.03	6.41 ± 0.18	1	120 × 120
16a-3	2.00 ± 0.03	5.06 ± 0.12	1	350 × 300
33	1.93 ± 0.03	4.65 ± 0.13	1	440 × 160
52-4-O	1.45 ± 0.04	6.16 ± 0.27	1	210 × 210
45	2.76 ± 0.03	5.09 ± 0.16	4	320 × 120
31	1.71 ± 0.04	7.80 ± 0.28	1	320 × 200
21412	1.49 ± 0.02	6.38 ± 0.14	1	200 × 140
54-7	2.15 ± 0.02	4.06 ± 0.94	4	180 × 150
51-1	1.98 ± 0.04	8.16 ± 0.26	1	380 × 340
51-8	1.64 ± 0.03	9.51 ± 0.19	1	570 × 570
55b-4	1.18 ± 0.02	7.58 ± 0.18	1	420 × 420
172†	1.92 ± 0.03	5.4 ± 0.2	1	200 × 160
2122-O†	2.09 ± 0.03	5.7 ± 0.2	1	160 × 160
2147†	1.99 ± 0.03	6.04 ± 0.17	1	160 × 160
8a-1†	2.03 ± 0.05	6.94 ± 0.29	1	160 × 120
13-1†	2.01 ± 0.04	5.08 ± 0.19	1	200 × 200
16a-2-lt†	1.96 ± 0.02	5.21 ± 0.11	1	200 × 200
19c-1†	1.97 ± 0.03	5.4 ± 0.2	1	200 × 200
52-11†	1.50 ± 0.03	6.09 ± 0.17	1	275 × 235
55b-2†	0.58 ± 0.03	5.9 ± 0.2	2	160 × 160
55b-3†	2.01 ± 0.05	5.79 ± 0.27	1	160 × 160

* Sizes determined from SE images of the grains, except as noted.
† Grains sputtered away during the measurements: sizes determined from NanoSIMS ion images; errors are 1σ.

spectra. Grain 21412 has Fe/O = 0.8 ± 0.1, while grain 54-7 has a ratio of 0.5 ± 0.1 (Table 2), using sensitivity factors derived from a hematite standard (Fe/O = 0.67). Within 2σ errors, grain 21412 has a composition consistent with FeO; a similar grain has been reported from the Acfer 094 carbonaceous chondrite (Floss et al., 2008).

3.1.5. Silicates

Most of the silicates have ferromagnesian compositions. In order to evaluate grain stoichiometries, (Mg + Fe ± Ca)/Si ratios were calculated (Fig. 6; Table 2); this ratio is 2 for olivine $(Mg,Fe)_2SiO_4$, and 1 for pyroxene $(Mg,Fe)SiO_3$. Fifteen grains have olivine-like compositions while ten grains have pyroxene-like compositions. Cation/O ratios provide additional constraints on the stoichiometries of the grains (Table 2). Only two of the pyroxene-like and eight of the olivine-like grains also contain O in stoichiometric proportions. In contrast, almost all olivine-like and pyroxene-like presolar silicates in the CR3 chondrites QUE 99177 and MET 00426 have O present in stoichiometric proportions (Floss and Stadermann, 2009a). The reason for the discrepancy is not clear, but we note that in virtually all cases the cation/O ratios are higher than the expected stoichiometric values (Table 2), indicating that excess O due to residual contamination is not the cause. Most of the silicates are Fe-rich with mg#s (Mg/[Mg + Fe]×100) < 60. However, two of the olivine-like grains have forsterite compositions (mg# = 100). Three of the pyroxene-like grains contain Al (5.8–7.3 at.%) and one contains Ca (~5 at.%); one grain contains both Al and Ca (Table 2).

Twenty-three silicates have (Mg + Fe ± Ca)/Si ratios that are intermediate between olivine and pyroxene (Fig. 6; Table 2). Again, most grains are Fe-rich (mg#s < 60), including one that contains no Mg (2-14-25-O2); of the Mg-rich grains, one contains no Fe (51-9). Seven of these grains also contain Ca (1.0–2.7 at.%) and/or Al (5.4–8.5 at.%). We note that Vollmer et al. (2009a) found that about half of the presolar silicates in Acfer 094 contained small (0.7–4.3 at.%) amounts of Ca; these authors attributed this to precipitation of carbonates during terrestrial alteration. The number of Ca-bearing grains is much less in this work, as well as in other presolar silicate studies (Floss and Stadermann, 2009a; Nguyen et al., 2010a), and terrestrial alteration in Antarctic meteorites is typically less severe than in hot desert meteorites (e.g., Crozaz et al., 2003). Nevertheless, there is some possibility that the Ca present in these grains is of terrestrial origin. Auger analyses of olivine and pyroxene standards show a Gaussian distribution in the measured compositions, with some overlap at intermediate compositions (Stadermann et al., 2009). However, the number of presolar grains with intermediate compositions that we observe in ALHA77307 is much larger than what is expected from the distribution of the standard grains, indicating that this is a real presolar grain population and not an artifact of the measurement technique.

Table 2
Elemental compositions (at.%) of presolar silicates and oxides in ALHA77307.

Grain name	Ca	O	Fe	Mg	Al	Si	mg#	(Fe + Mg ± Ca)/Si	Cation/O
Pyroxene-like silicates*								1	0.67
133	–	63.1 ± 2.3	–	18.5 ± 1.7	–	18.4 ± 2.0	100	1.0 ± 0.1	0.58 ± 0.05
5b-7	*1.9 ± 0.2*	*52.4 ± 1.9*	*13.9 ± 1.6*	*5.6 ± 0.5*	*5.8 ± 1.4*	*20.4 ± 2.2*	*29*	*1.0 ± 0.1*	*0.9 ± 0.1*
10-4-tp	–	*55.1 ± 2.0*	*16.6 ± 1.9*	*5.3 ± 0.5*	–	*23.0 ± 2.5*	*24*	*1.0 ± 0.1*	*0.8 ± 0.1*
11-1-lt	–	*54.7 ± 2.0*	*12.3 ± 1.4*	*8.7 ± 0.8*	*7.3 ± 1.8*	*17.0 ± 1.9*	*41*	*1.2 ± 0.2*	*0.8 ± 0.1*
11-1-rt	–	*52.7 ± 1.9*	*12.7 ± 1.4*	*9.7 ± 0.9*	–	*24.9 ± 2.7*	*43*	*0.9 ± 0.1*	*0.9 ± 0.1*
15-5-bm	–	*54.9 ± 2.0*	*11.5 ± 1.3*	*9.8 ± 0.9*	*6.0 ± 1.5*	*17.8 ± 2.0*	*46*	*1.2 ± 0.2*	*0.8 ± 0.1*
18-6	–	59.8 ± 2.2	13.6 ± 1.5	8.2 ± 0.8	–	18.4 ± 2.0	38	1.2 ± 0.2	0.7 ± 0.1
18-7	–	*54.8 ± 2.0*	*11.4 ± 1.3*	*10.9 ± 1.0*	–	*22.9 ± 2.5*	*49*	*1.0 ± 0.1*	*0.8 ± 0.1*
54-1	*4.9 ± 0.5*	*54.6 ± 2.0*	*11.8 ± 1.3*	*6.3 ± 0.6*	–	*22.4 ± 2.5*	*35*	*1.0 ± 0.1*	*0.8 ± 0.1*
48-bm	–	*53.9 ± 1.9*	*14.2 ± 1.6*	*7.6 ± 0.7*	*5.8 ± 1.4*	*18.5 ± 2.0*	*35*	*1.2 ± 0.2*	*0.9 ± 0.1*
Olivine-like silicates*								2	0.75
1310	–	*53.4 ± 1.9*	*16.3 ± 1.8*	*13.9 ± 1.3*	–	*16.4 ± 1.8*	*46*	*1.8 ± 0.2*	*0.9 ± 0.1*
5b-8	–	59.2 ± 2.1	20.8 ± 2.3	6.3 ± 0.6	–	13.6 ± 1.5	23	2.0 ± 0.3	0.7 ± 0.1
63	–	55.0 ± 2.0	14.7 ± 1.6	15.9 ± 1.5	–	14.4 ± 1.6	52	2.1 ± 0.3	0.8 ± 0.1
8a-4-bm	–	*62.6 ± 2.3*	–	*25.5 ± 2.4*	–	*11.9 ± 1.3*	*100*	*2.1 ± 0.3*	*0.60 ± 0.05*
10-4-O18	–	55.1 ± 2.0	12.9 ± 1.4	16.7 ± 1.6	–	15.3 ± 1.7	56	1.9 ± 0.3	0.8 ± 0.1
114	–	*49.9 ± 1.8*	*20.6 ± 2.3*	*13.1 ± 1.2*	–	*16.3 ± 1.8*	*39*	*2.1 ± 0.3*	*1.0 ± 0.1*
116	–	55.0 ± 2.0	25.8 ± 2.9	4.5 ± 0.4	–	14.7 ± 1.6	15	2.1 ± 0.3	0.8 ± 0.1
12-4	–	*49.7 ± 1.8*	*21.1 ± 2.4*	*13.5 ± 1.3*	–	*15.6 ± 1.7*	*39*	*2.2 ± 0.3*	*1.0 ± 0.1*
128	–	56.6 ± 2.0	13.8 ± 1.5	15.1 ± 1.4	–	14.6 ± 1.6	52	2.0 ± 0.3	0.8 ± 0.1
17b-2	–	57.7 ± 2.1	15.3 ± 1.7	11.9 ± 1.1	–	15.0 ± 1.7	44	1.8 ± 0.2	0.7 ± 0.1
51-6-O17	–	*52.2 ± 1.9*	*10.3 ± 1.2*	*21.5 ± 2.0*	–	*16.0 ± 1.8*	*68*	*2.0 ± 0.3*	*0.9 ± 0.1*
52-15	–	55.8 ± 2.0	–	29.8 ± 2.8	–	14.4 ± 1.6	100	2.1 ± 0.3	0.8 ± 0.1
53-5	–	*52.1 ± 1.9*	*16.8 ± 1.9*	*16.5 ± 1.6*	–	*14.6 ± 1.6*	*50*	*2.3 ± 0.3*	*0.9 ± 0.1*
53-11	–	56.8 ± 2.0	13.3 ± 1.5	16.7 ± 1.6	–	13.3 ± 1.5	56	2.3 ± 0.3	0.8 ± 0.1
54-9	–	*53.2 ± 1.9*	*11.6 ± 1.3*	*18.6 ± 1.7*	–	*16.6 ± 1.8*	*62*	*1.8 ± 0.2*	*0.9 ± 0.1*
Intermediate silicates									
111-O	–	55.2 ± 2.0	16.9 ± 1.9	7.2 ± 0.7	6.4 ± 1.6	14.3 ± 1.6	30	1.7 ± 0.2	0.8 ± 0.1
112	–	57.3 ± 2.1	11.0 ± 1.2	14.7 ± 1.4	–	17.1 ± 1.9	57	1.5 ± 0.2	0.7 ± 0.1
1-24	–	55.9 ± 2.0	16.6 ± 1.9	11.1 ± 1.0	–	16.4 ± 1.8	40	1.7 ± 0.2	0.8 ± 0.1
132	–	57.8 ± 2.1	13.4 ± 1.5	11.7 ± 1.1	–	17.1 ± 1.9	47	1.5 ± 0.2	0.7 ± 0.1
146	–	56.5 ± 2.0	10.6 ± 1.2	14.9 ± 1.4	–	18.0 ± 2.0	58	1.4 ± 0.2	0.8 ± 0.1
178	1.0 ± 0.1	54.6 ± 2.0	12.6 ± 1.4	9.9 ± 0.9	5.3 ± 1.3	16.6 ± 1.8	44	1.4 ± 0.2	0.8 ± 0.1
2131	–	59.3 ± 2.1	12.1 ± 1.4	11.2 ± 1.1	–	17.3 ± 1.9	48	1.3 ± 0.2	0.69 ± 0.05
21422	–	59.8 ± 2.2	20.2 ± 2.3	4.5 ± 0.4	–	15.5 ± 1.7	18	1.6 ± 0.2	0.7 ± 0.1
2-1425-O	–	57.2 ± 2.1	25.1 ± 2.8	–	–	17.7 ± 1.9	0	1.4 ± 0.2	0.7 ± 0.1
32	1.3 ± 0.1	59.1 ± 2.1	9.2 ± 1.0	14.6 ± 1.4	–	15.8 ± 1.7	61	1.6 ± 0.2	0.69 ± 0.05
42	–	60.7 ± 2.2	20.7 ± 2.3	4.2 ± 0.4	–	14.5 ± 1.6	17	1.7 ± 0.2	0.6 ± 0.1
44-O	1.0 ± 0.1	57.9 ± 2.1	8.5 ± 1.0	14.6 ± 1.4	–	17.9 ± 2.0	63	1.3 ± 0.2	0.7 ± 0.1
48-tp	–	58.7 ± 2.1	14.2 ± 1.6	9.9 ± 0.9	–	17.2 ± 1.9	41	1.4 ± 0.2	0.7 ± 0.1
410	1.2 ± 0.1	57.1 ± 2.1	20.6 ± 2.3	5.0 ± 0.5	–	16.0 ± 1.8	20	1.7 ± 0.2	0.7 ± 0.1
7d-2	–	56.9 ± 2.0	15.0 ± 1.7	10.8 ± 1.0	–	17.3 ± 1.9	42	1.5 ± 0.2	0.8 ± 0.1
8a-3-O17	–	55.0 ± 2.0	17.7 ± 2.0	10.3 ± 1.0	–	17.0 ± 1.9	37	1.6 ± 0.2	0.8 ± 0.1

107	–	50.1 ± 1.8	17.1 ± 1.9	14.2 ± 1.3	–	18.6 ± 2.0	45	1.7 ± 0.2	1.0 ± 0.1
113	–	51.7 ± 1.9	12.3 ± 1.4	11.7 ± 1.1	5.4 ± 1.3	19.0 ± 2.1	49	1.3 ± 0.2	0.9 ± 0.1
13-4	–	50.3 ± 1.8	17.4 ± 1.9	14.0 ± 1.3	–	18.2 ± 2.0	45	1.7 ± 0.2	1.0 ± 0.1
15-5-tp	2.7 ± 0.3	54.9 ± 2.0	10.0 ± 1.1	8.8 ± 0.8	8.5 ± 2.1	15.2 ± 1.7	47	1.4 ± 0.2	0.8 ± 0.1
51-7	–	57.2 ± 2.1	7.5 ± 0.8	16.9 ± 1.6	–	18.4 ± 2.0	69	1.3 ± 0.2	0.7 ± 0.1
51-9	–	55.1 ± 2.0	–	25.8 ± 2.4	–	19.1 ± 2.1	100	1.4 ± 0.2	0.8 ± 0.1
53-4	–	63.2 ± 2.3	13.3 ± 1.5	8.4 ± 0.8	–	15.1 ± 1.7	39	1.4 ± 0.2	0.58 ± 0.04
Other silicates									
131	–	62.8 ± 2.3	–	15.3 ± 1.4	–	21.8 ± 2.4	100	0.7 ± 0.1	0.59 ± 0.05
163	–	62.0 ± 2.2	9.2 ± 1.0	6.3 ± 0.6	–	22.6 ± 2.5	41	0.7 ± 0.1	0.61 ± 0.05
1710	–	62.9 ± 2.3	–	14.4 ± 1.4	–	22.7 ± 2.5	100	0.6 ± 0.1	0.59 ± 0.05
105	2.1 ± 0.2	59.7 ± 2.1	8.0 ± 0.9	–	9.3 ± 2.3	20.8 ± 2.3	0	0.5 ± 0.1	0.7 ± 0.1
13-5	–	60.6 ± 2.2	–	15.6 ± 1.5	–	23.8 ± 2.6	100	0.7 ± 0.1	0.7 ± 0.1
2-1425-O1	–	55.8 ± 2.0	18.7 ± 2.1	–	–	25.4 ± 2.8	0	0.7 ± 0.1	0.8 ± 0.1
19-1	3.4 ± 0.4	61.0 ± 2.2	–	11.0 ± 1.0	–	24.6 ± 2.7	100	0.6 ± 0.1	0.6 ± 0.1
16a-3	–	53.6 ± 1.9	8.8 ± 1.0	6.8 ± 0.6	6.4 ± 1.6	24.3 ± 2.7	44	0.6 ± 0.1	0.9 ± 0.1
44-O17	–	51.4 ± 1.9	21.1 ± 2.4	13.8 ± 1.3	–	13.7 ± 1.5	40	2.5 ± 0.3	0.9 ± 0.1
8a-3-O	1.1 ± 0.1	56.5 ± 2.0	10.6 ± 1.2	19.2 ± 1.8	–	12.6 ± 1.4	64	2.5 ± 0.3	0.8 ± 0.1
8a-4-tp	–	62.8 ± 2.3	17.8 ± 2.0	8.6 ± 0.8	–	10.8 ± 1.2	33	2.4 ± 0.3	0.59 ± 0.04
121	–	54.7 ± 2.0	14.2 ± 1.6	17.7 ± 1.7	–	13.4 ± 1.5	55	2.4 ± 0.3	0.8 ± 0.1
127	–	55.9 ± 2.0	16.4 ± 1.8	16.0 ± 1.5	–	11.6 ± 1.3	49	2.8 ± 0.4	0.8 ± 0.1
51-6-O	–	55.3 ± 2.0	16.3 ± 1.8	17.5 ± 1.6	–	10.9 ± 1.2	52	3.1 ± 0.4	0.8 ± 0.1
52-8	–	52.2 ± 1.9	19.5 ± 2.2	14.7 ± 1.4	–	13.6 ± 1.5	43	2.5 ± 0.3	0.9 ± 0.1
53-6	–	51.6 ± 1.9	19.5 ± 2.2	17.6 ± 1.7	–	11.4 ± 1.3	47	3.3 ± 0.4	0.9 ± 0.1
54-5	3.5 ± 0.4	58.1 ± 2.1	14.0 ± 1.6	11.3 ± 1.1	–	13.0 ± 1.4	45	2.2 ± 0.3	0.72 ± 0.05
52-4-O17	–	44.9 ± 1.6	20.4 ± 2.3	9.9 ± 0.9	8.2 ± 2.0	16.5 ± 1.8	33	1.8 ± 0.3	1.2 ± 0.1
33	–	51.1 ± 1.8	30.1 ± 3.4	5.0 ± 0.5	9.3 ± 2.3	4.5 ± 0.5	14	7.8 ± 1.1	1.0 ± 0.1
Silica									
10-4-bm	–	65.4 ± 2.4	–	–	–	34.6 ± 3.8	–	–	0.5 ± 0.1
2132	–	69.1 ± 2.5	–	–	–	30.9 ± 3.4	–	–	0.4 ± 0.1
21420	–	69.1 ± 2.5	–	–	–	30.9 ± 3.4	–	–	0.4 ± 0.1
Al oxides									
52-4-O	–	65.4 ± 2.4	–	–	34.6 ± 8.6	–	–	–	0.5 ± 0.1
45	–	75.0 ± 2.7	–	–	25.0 ± 6.2	–	–	–	0.4 ± 0.1
31	–	74.4 ± 2.7	–	–	25.6 ± 6.4	–	–	–	0.4 ± 0.1
Fe oxides									
21412	–	55.6 ± 2.0	44.4 ± 5.0	–	–	–	–	–	0.8 ± 0.1
54-7	–	66.7 ± 2.4	33.3 ± 3.7	–	–	–	–	–	0.5 ± 0.1
Mg oxide									
55b-4	–	49.2 ± 1.8	–	50.8 ± 4.8	–	–	–	–	1.0 ± 0.1
Composite grains									
51-1(tp)	–	44.7 ± 1.6	27.5 ± 3.1	13 ± 1.2	–	14.8 ± 1.6	32	2.7 ± 0.4	1.2 ± 0.1
51-1(bm)	–	50.5 ± 1.8	18.2 ± 2.0	15.0 ± 1.4	–	16.3 ± 1.8	33	2.0 ± 0.3	1.0 ± 0.1
51-8 (lt)	3.9 ± 0.4	57.4 ± 2.1	8.4 ± 0.9	8.8 ± 0.8	–	21.5 ± 2.4	51	1.0 ± 0.1	0.7 ± 0.1
51-8 (rt)	–	53.8 ± 1.9	15.2 ± 1.7	11.9 ± 1.1	–	19.1 ± 2.1	44	1.4 ± 0.2	0.9 ± 0.1

* Grains in italics do not have O in stoichiometric proportions (see text for details); mg#: Mg/(Mg+Fe)*100; errors are 1σ.

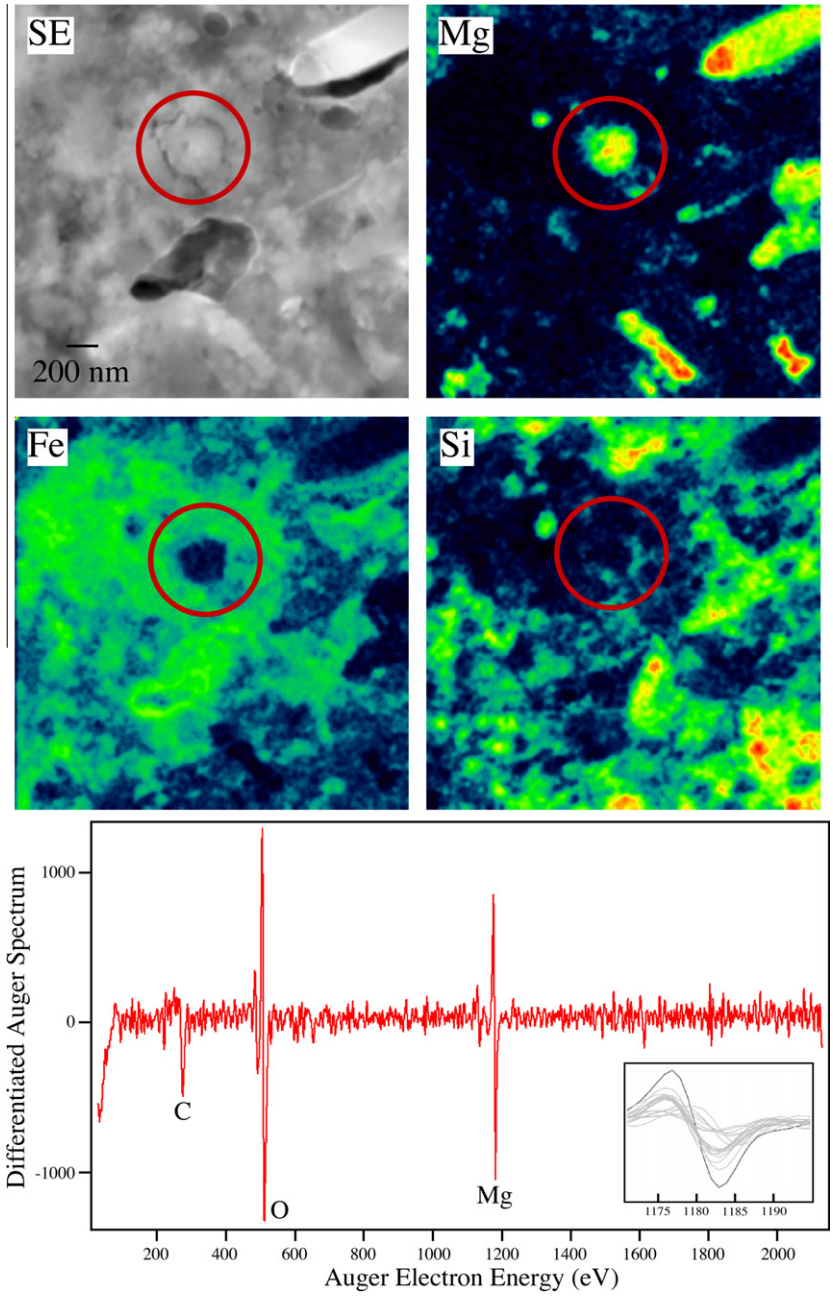

Fig. 2. Secondary electron image, Mg, Fe, and Si elemental maps, and Auger spectrum of grain 55b-4 (C is due to surface contamination). The inset shows the Mg peak of the grain (black) compared to the Mg peaks in ferromagnesian silicates (gray; scaled to the O peak-to-peak height of 55b-4).

Other non-stoichiometric silicates (listed under "other" in Table 2) include grains with $(Mg + Fe \pm Ca)/Si$ ratios > 2 and those with $(Mg + Fe \pm Ca)/Si$ ratios < 1. Five contain Ca and/or Al and several grains are Si-rich (~25 at.%) compared to the stoichiometric silicates, while one is Si-poor (~5 at.%) and has a high Al abundance (~9 at.%; Table 2).

3.1.6. Composite grains

Two relatively large (~400 × 400 nm^2) composite grains are also present in our silicate grain inventory and are described below.

Grain 51-8 is a Group 1 grain consisting of multiple subgrains (Fig. 7). The $\delta^{17}O$ image is uniform throughout, but the $\delta^{18}O$ image shows some minor heterogeneity. The secondary electron image shows that the lower-left part of the composite grain is a single compact grain, while the upper-right area consists of multiple subgrains that are ~50–70 nm in diameter and have near-circular shapes. Elemental spectra were acquired for each region, listed as left (lt) and right (rt) in Table 2 and Fig. 7. The left part of grain 51-8 contains 3.9 ± 0.4 at.% Ca and has a pyroxene-like composition (Table 2). No Ca is present in the region on the right, but this area has

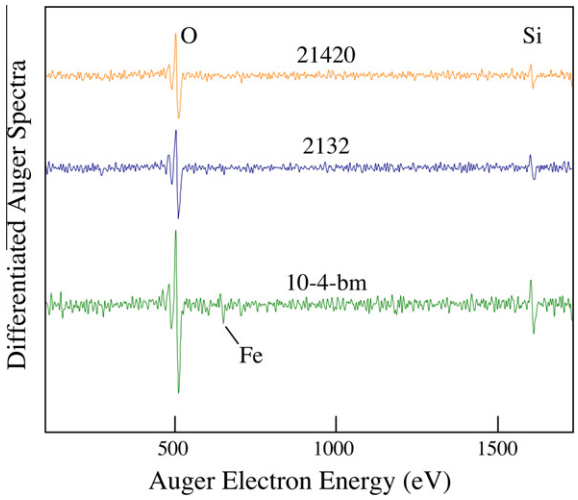

Fig. 3. Auger spectra of silica grains 21420, 2132, and 10-4-bm. The small Fe peak in grain 10-4-bm is due to backscattered Auger electrons from an Fe-rich region adjacent to the grain.

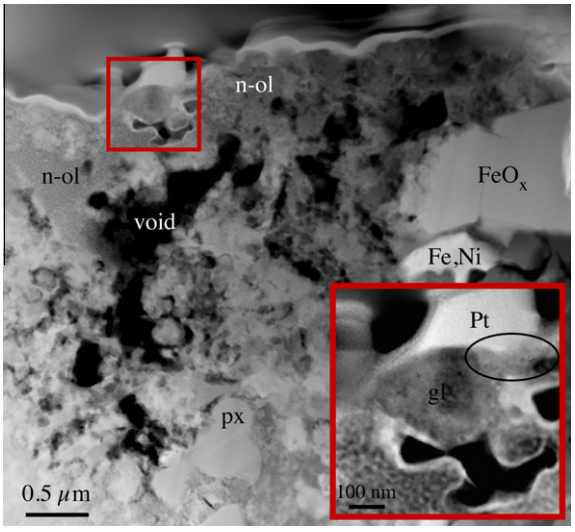

Fig. 4. Annular dark-field scanning transmission electron microscopy image of grain 21420 and surrounding matrix. The grain is marked with a black ellipse. Pt: FIB-deposited platinum; n-ol: nanoscale Fe-rich olivine; gl: Mg-rich glass; px: Mg-rich pyroxene.

a higher Fe abundance and a non-stoichiometric elemental composition.

The second composite grain, 51-1, is uniformly enriched in ^{17}O, with normal $^{18}O/^{16}O$ (Group 1) and consists of two subgrains (Fig. 8). The upper grain (51-1-tp) is ~200 nm in diameter while the lower one (51-1-bm) is 160 × 140 nm^2 in size. The spectra show that both subgrains are composed predominantly of Fe, Mg, Si, and O. The bottom subgrain exhibits an olivine-like composition while the top one again has a significantly higher Fe abundance and a non-stoichiometric composition (Table 2).

3.2. Isotopic and elemental compositions of C- and N-anomalous grains

In addition to the O-anomalous grains, we identified 22 C-anomalous grains from the C,O imaging and 47 C- and/or N-anomalous grains from the C,N imaging (Tables 3 and 4; Fig. 9). The majority of the grains were classified as either SiC or carbonaceous, based on the Auger Nanoprobe measurements. Classification of some grains, which had sputtered away or could not be relocated due to image alignment difficulties, was based on the isotopic data and from the $^{12}C^-/^{28}Si^-$ ratios derived from the NanoSIMS ion images (see below).

3.2.1. SiC grains

We identified 25 SiC grains, resulting in a calculated abundance of 110 ± 20 ppm for this meteorite. The $^{12}C/^{13}C$ ratios of the grains vary from ~4 to 75; one grain has a higher than terrestrial ratio of 111 ± 4 (Fig. 9; Table 3). The $^{14}N/^{15}N$ ratios range from ~245 to 810. Representative Auger spectra and an elemental distribution map are shown in Fig. 10. Most grains are roughly circular in shape and range in size from ~100 nm to 500 nm. Some grains could not be characterized in the Auger Nanoprobe and were identified on the basis of NanoSIMS isotopic and/or elemental ratios (Table 3). Although the detection efficiencies of the electron multipliers can vary between different sets of measurements and, as a consequence, lead to some uncertainty in the measured $^{12}C^-/^{28}Si^-$ ratio, the ratios (0.5–1.7) for SiC are significantly lower than those (1–65) for the carbonaceous phases (e.g., Floss and Stadermann, 2009b). Oxygen is often present in the Auger spectra of the SiC grains. Calculation of the O contents associated with the SiC shows ~10 at.% O for the larger grains. SiC forms a thin oxidized layer on its surface upon exposure to air and this likely accounts for much of the O observed, as we also see such O peaks in the Auger spectra of isolated SiC grains on high purity Au mounts. However, other factors such as residual surface contamination or the backscatter effect (Stadermann et al., 2009) may also play a role, particularly for smaller grains.

3.2.2. Carbonaceous grains

We identified twenty-eight areas enriched in ^{15}N, with $\delta^{15}N$ values from 410–1265‰ (Fig. 9; Table 4); the calculated abundance is 160 ± 30 ppm. Three of these areas (D1, E7-tp and F1-17) also show ^{13}C excesses. Table 4 lists the elements present in these grains in decreasing order abundance. The Auger spectra typically show large C and O peaks; some spectra also show the presence of Mg, Si and Fe, due to silicates embedded in or intermixed with the N-anomalous material, much of which is quite porous. Minor S is also present in some of the N-anomalous hotspots (Table 4). Nitrogen is below detection (<3 at.%) in all but one of the C- and N-anomalous grains. Four C-anomalous grains (146, 21414, 21419, 51) with $^{12}C/^{13}C$ ratios > 89 (Table 4) could not be classified. Based on the fact that most carbonaceous grains are ^{12}C-rich (Floss and Stadermann, 2009b) whereas most SiC grains are ^{13}C

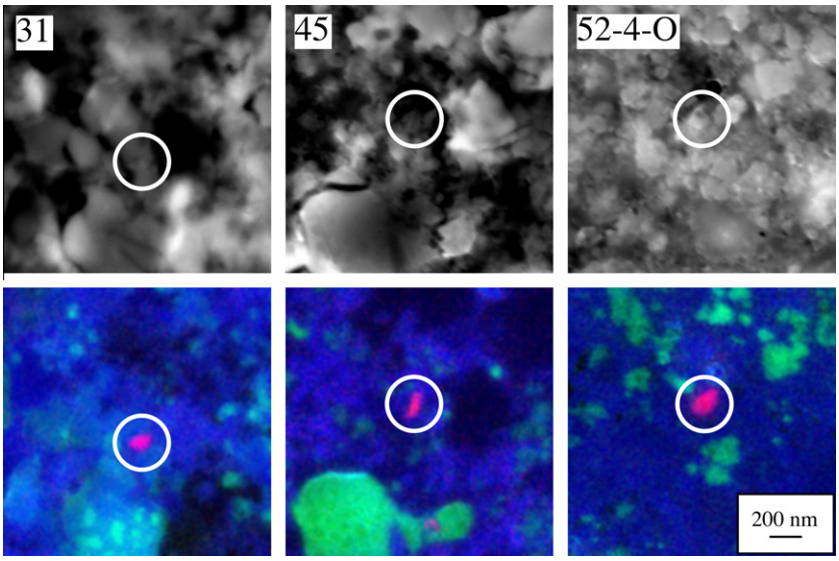

Fig. 5. Secondary electron and RGB (Red = Al; Green = Mg; Blue = O) images of Al-oxide grains. (For interpretation of the references to color in this figure legend, the reader is referred to the web version of this article.)

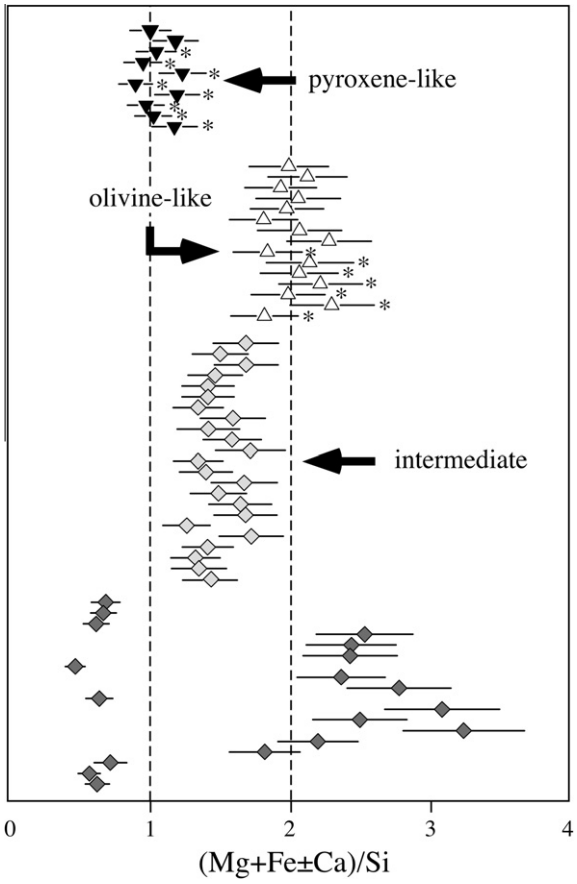

Fig. 6. (Mg + Fe ± Ca)/Si ratios of ALHA77307 ferromagnesian silicates. Pyroxene-like and olivine-like grains with non-stoichiometric cation/O ratios are shown with an asterisk (∗). One grain with a (Mg + Fe)/Si ratio of ~8, is not shown.

rich, it seems likely that these grains are carbonaceous. The carbonaceous grains are generally somewhat larger than the SiC grains (Table 4) and are often irregular in shape; however, some of the ^{15}N-rich hotspots are nanoglobules with circular shapes and hollow structures, while others appear smooth and platy or compact (Fig. 11). One ^{15}N-rich area, G4, occurs as a rim surrounding a large (~1 μm) grain with a platy, flat appearance (Fig. 12). The host grain contains Fe, Ni and C and has a solar C isotopic composition. The N-anomalous rim is C-rich and partially coats the platy grain.

4. DISCUSSION

4.1. Stellar sources of O-anomalous grains

As noted above, the O-anomalous grains in our inventory fall into the four groups initially defined by Nittler et al. (1997) for presolar oxides (Fig. 1). Group 1 grains with ^{17}O excesses and solar to sub-solar ^{18}O/^{16}O ratios, make up the majority of the O-anomalous grain inventory. Low-mass stars (1.1–2.2$M_{\odot}$) of close-to-solar metallicity in the thermally pulsing AGB phase of evolution are the likely sources of these grains (e.g., Nittler et al., 1997, 2008; Gail et al., 2009). The isotopic compositions of these grains show the signature of first and/or second dredge-up episodes that bring ^{17}O-rich material formed during the H-burning phase into the stellar envelope (Nittler et al., 2008). Low-mass AGB stars undergoing dredge-up episodes cannot account for the large ^{18}O depletions (^{18}O/^{16}O $< \sim 10^{-3}$) of Group 2 grains. However, their compositions can be understood by assuming an additional process called cool bottom processing (Wasserburg et al., 1995), during which deep circulation transports material from the envelope through hot H-burning regions to partially process the material, destroying ^{18}O in the process (Nollett et al., 2003). Nittler et al. (2008) suggested that some of the spread in the ^{18}O/^{16}O ratios of Group 1 grains may also reflect the effects of CBP. Finally, ^{16}O-rich Group 3 grains, like the one in

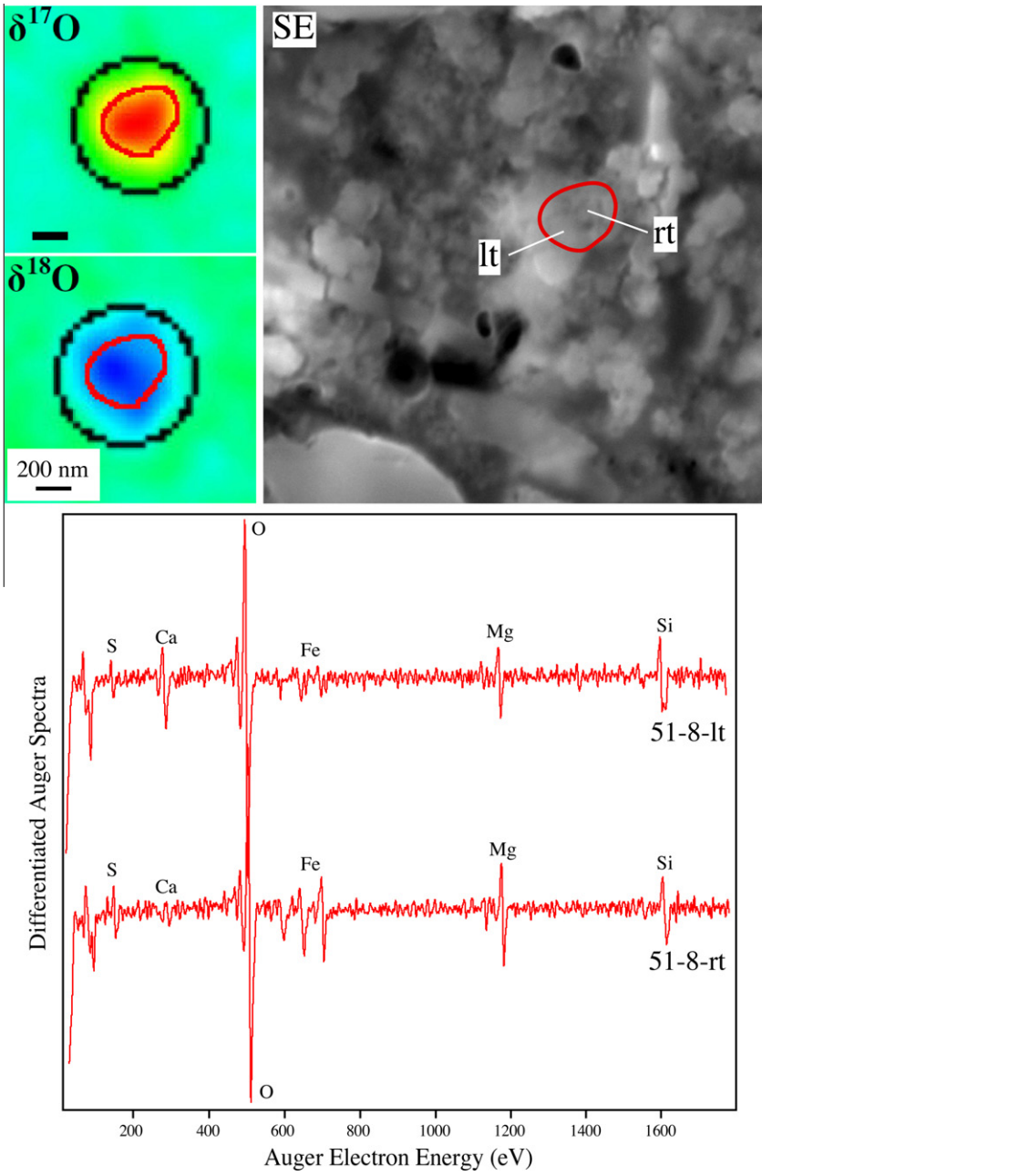

Fig. 7. Composite grain 51-8. The O isotopic anomaly is outlined in the $\delta^{17}O$, $\delta^{18}O$ and SE images. Auger spectra are shown for the left (lt) and right (rt) parts of the grain.

our inventory (Table 1, Fig. 1), also have likely origins in low-mass AGB stars, but some Group 3 grains that fall below the galactic chemical evolution (GCE) line and Group 4 grains with ^{18}O enrichments probably originate in Type II supernovae (Nittler et al., 2008).

A few Group 1 grains, including one in our inventory (Fig. 1), have $^{17}O/^{16}O$ ratios that are higher than can be accounted for by nucleosynthesis and dredge-up in low-mass AGB stars ($>\sim 6 \times 10^{-3}$; Gyngard et al., 2011). It has been suggested that these so-called 'extreme Group 1' grains, have nova origins (Nittler and Hoppe, 2005) and, indeed, early model predictions for novae were consistent with the very high $^{17}O/^{16}O$ ratios of these grains (José et al., 2004). However, more recent calculations, using updated reaction rates indicate that the predicted O isotopic compositions do not match the grain data unless a large amount of mixing with solar system composition material is included (Gyngard et al., 2010a, 2011). These nova models also predict large anomalies in elements such as Mg and Si. However, while a few 'extreme Group 1' grains show modest enrichments in the heavy isotopes of Si and Mg (Vollmer et al., 2008; Gyngard et al., 2010a,b; 2011), much larger enrichments are predicted (José et al., 2004; Gyngard et al., 2010a, 2011). Additional modeling efforts and more

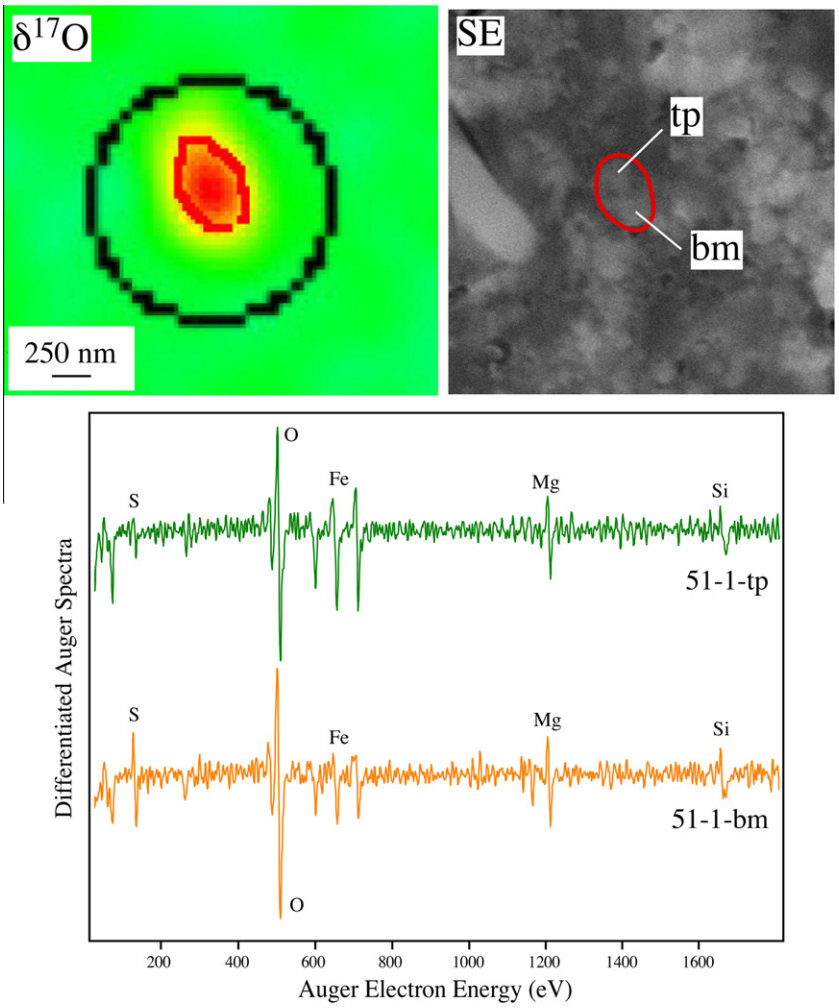

Fig. 8. Composite grain 51-1. The O isotopic anomaly is outlined in the $\delta^{17}O$ and SE images. Auger spectra are shown for the top (tp) and bottom (bm) parts of the grain.

^{17}O-rich grains on which multi-element isotopic analyses can be carried out are clearly needed to understand the origins of these grains. Given the very large discrepancies in several isotopic systems, it is possible that these grains don't come from novae at all (e.g., Nittler et al., 2008).

4.2. Elemental compositions of O-anomalous grains

4.2.1. Ferromagnesian silicates

Grains with ferromagnesian compositions dominate the presolar silicate inventory in ALHA77307 as well as in other primitive meteorites with abundant presolar grains, making up between 85 and 95% of all the O-anomalous grains identified (e.g., Nguyen et al., 2007, 2010a; Floss and Stadermann, 2009a, 2012; Vollmer et al., 2009a; Bose et al., 2010c; this study). Approximately 1/3 of these are grains whose compositions are consistent with either olivine or pyroxene, while the remaining grains are non-stoichiometric, many of them with compositions intermediate between olivine and pyroxene or (e.g., Fig. 6). Irradiation, shock and sputtering processes in the interstellar medium can induce changes in the structures, chemical compositions, and porosities of presolar grains (Demyk et al., 2001; Carrez et al., 2002) and may play a role in transforming stoichiometric grains into grains with non-stoichiometric compositions (Min et al., 2007; Keller and Messenger, 2011). An alternative possibility is that these non-stoichiometric compositions are primary and are the result of condensation of the grains under kinetic conditions. As noted above, TEM studies show that many presolar silicates exhibit heterogeneous structures and have variable compositions (Stroud et al., 2009; Vollmer et al., 2009b), most likely as the result of complex formation in non-equilibrium environments. This is also consistent with astronomical observations that most circumstellar silicates are amorphous, with crystalline silicates typically making up less than 10% of stellar condensates (Tielens et al., 1998; Kemper et al., 2001). Moreover, recent modeling work on the formation of dust in O-rich stars has shown that most silicate dust is formed during short high-mass-loss episodes that occur after thermal pulses in thermally pulsing AGB stars (Gail et al., 2009). The stellar environment during

Table 3
Presolar SiC in ALHA77307.*

Grain name	$^{12}C/^{13}C$	$\delta^{13}C$ (‰)	$^{14}N/^{15}N$	$\delta^{15}N$ (‰)	Type*	C^-/Si^-	Size (nm)
1211	28.6 ± 0.7	2110 ± 25	–	–	ms	–	200 × 200
139	48.2 ± 1.6	845 ± 35	–	–	ms	–	200 × 200
172	43.2 ± 0.8	1060 ± 20	–	–	ms	–	430 × 350
2136	60.8 ± 2.4	465 ± 40	–	–	ms	–	160 × 160
2141	50.2 ± 0.8	775 ± 20	–	–	ms	–	235 × 235
2148	57.5 ± 1.2	550 ± 20	–	–	ms	–	235 × 235
21418	21.1 ± 0.1	3220 ± 6	–	–	ms	–	420 × 290
2142	71.6 ± 2.6	240 ± 40	–	–	ms	–	160 × 120
5a1	54.8 ± 0.5	625 ± 10	–	–	ms	–	500 × 400
5b4	52.5 ± 0.9	695 ± 20	–	–	ms	–	350 × 275
8a1	34.8 ± 0.5	1560 ± 15	–	–	ms	–	350 × 315
106	4.28 ± 0.04	19750 ± 10	–	–	A + B	–	390 × 390
111lt	53.7 ± 0.8	655 ± 15	–	–	ms	–	430 × 400
111rt	18.2 ± 0.5	3880 ± 35	–	–	ms	–	200 × 160
136	11.6 ± 0.2	6695 ± 15	–	–	ms	–	470 × 390
151	57.8 ± 1.0	540 ± 20	–	–	ms	–	110 × 110
52-17	37.0 ± 2.4	1410 ± 75	–	–	ms	–	125 × 125
53-9	13.5 ± 0.5	5620 ± 40	–	–	ms	–	110 × 90
B2	111.0 ± 3.7	-200 ± 35	273.4 ± 23.3	-5 ± 93	Y	1.7	200 × 170
D2	63.7 ± 1.4	400 ± 30	401.0 ± 23.2	-322 ± 60	ms	1.1	260 × 240
D4	55.2 ± 1.9	610 ± 55	244.7 ± 19.1	111 ± 85	ms	1.3	140 × 110
E1	51.5 ± 1.0	730 ± 35	413.8 ± 34.7	-343 ± 88	ms	1.1	230 × 170
G2-lt	74.7 ± 2.0	190 ± 30	810.5 ± 70.7	-664 ± 90	ms	0.8	310 × 140
G2-tp	64.5 ± 1.2	380 ± 25	517.5 ± 57.2	-474 ± 117	ms	0.8	390 × 270
G7-bm	20.3 ± 0.8	3390 ± 160	403.1 ± 86.1	-325 ± 244	ms	0.5	510 × 280

* Grains in italics were identified only on the basis of NanoSIMS isotopic data; ms: mainstream; errors are 1σ (errors for C^-/Si^- ratios range from 0.01–0.5).

these episodes will be highly variable, with strong stellar winds and rapid temperature drops, leading to grain formation under kinetic conditions. It is likely that both processes play a role in the elemental compositions that we observe.

We examined the available presolar ferromagnesian silicate data to look for correlations between isotopic and elemental compositions in the grains. As shown in Fig. 13, we observe a significant compositional difference between grains from different stellar sources; Groups 3 and 4 contain significantly more grains with olivine(-like) compositions than Groups 1 and 2. The olivine/pyroxene ratio in Groups 3 and 4 grains, of likely supernova origin, is ~3, while Groups 1 and 2 grains, thought to come from AGB stars, contain approximately equal proportions of olivine and pyroxene compositions (Fig. 13). Some Group 3 grains probably have AGB origins (Nittler et al., 2008), but the results are not significantly affected if these are added to Groups 1 and 2, rather than Group 4, due to the small number of these grains overall. Olivine is the first major silicate expected to condense from a gas of solar composition (Lodders and Fegley, 1999) and, thus, olivine compositions among presolar silicates are not unexpected. However, it is not obvious why supernovae should produce more olivine than O-rich AGB stars. A possible explanation for the difference may be found by considering the possibility of a supernova explosion in close proximity to the early solar system (e.g., Ouellette et al., 2009). Nittler et al. (2008) have noted that the isotopic compositions of most Group 4 grains are consistent with a single mixing line, suggesting a single source for these grains. In addition, Group 4 grains appear to be overabundant (~35%) in IDPs and Antarctic micrometeorites, but underabundant (~3%) in CR3 chondrites (Floss and Stadermann, 2009a), compared to the overall presolar silicate and oxide population (~10%; Yada et al., 2008). These heterogeneities could be explained by injection of the Group 4 grains into the early solar nebula by a single supernova (Nittler et al., 2008), with the result that materials accreting in different parts of the nebula, or at different times, incorporated different proportions of these grains. Grain lifetimes in the interstellar medium are shorter than the rate at which grains are replenished from stellar sources (Tielens, 1998). If presolar grains were, in fact, injected into the early solar nebula by a nearby supernova, these grains would likely have been incorporated into primitive solar system materials before alteration of their compositions and/or structures through irradiation and sputtering processes in the ISM, implying that the high proportion of olivine to pyroxene compositions that we observe among the Group 4 grains reflects their initial relative abundances at the time of incorporation into the solar nebula. Groups 1 and 2 grains, in contrast, are more likely to reflect a combination of initial grain compositions and changes due to secondary processing as the grains traversed the interstellar medium. Such a scenario is, of course, highly speculative, but is consistent with other models favoring supernova injection, for example to account for the presence of short-lived radionuclides into the early solar system (Ouellette et al., 2009).

Table 4
Carbonaceous phases in ALHA77307.

Grain name	$^{12}C/^{13}C$	$\delta^{13}C$ (‰)	$^{14}N/^{15}N$	$\delta^{15}N$ (‰)	Elements*	C^-/Si^-	Size (nm)
D1†	85.3 ± 0.6	45 ± 10	187.1 ± 3.4	454 ± 19	C,O,S	25	580 × 360
D6	87.3 ± 1.7	20 ± 20	139.2 ± 6.4	954 ± 50	O,C,Mg,Si	3	220 × 200
D8	88.9 ± 0.8	1 ± 10	135.8 ± 2.8	1003 ± 21	C,O,Fe,S	36	480 × 460
E2	89.2 ± 0.8	−2 ± 10	179.1 ± 4.5	519 ± 26	C,O	11	460 × 290
E4-lt	86.0 ± 0.7	35 ± 10	174.1 ± 3.1	563 ± 18	C,O	30	420 × 380
E4-rt	88.1 ± 0.6	10 ± 5	173.7 ± 4.4	566 ± 26	O,C,Fe	20	660 × 330
E7-bm	88.9 ± 0.9	1 ± 10	192.9 ± 10.1	410 ± 56	C,O	62	800 × 400
E7-tp†	83.2 ± 1.0	70 ± 10	188.7 ± 10.8	442 ± 62	C,O	38	380 × 300
E7-lt†	88.3 ± 1.9	7 ± 20	181.4 ± 7.8	499 ± 46	C,O,Fe,S	12	200 × 160
E7-rt	90.3 ± 2.3	−15 ± 25	187.8 ± 12.9	448 ± 75	O,C,Fe,Si,Mg	6	140 × 80
E9-lt	89.0 ± 1.7	0 ± 20	178.6 ± 9.2	523 ± 56	C,O,Al,Fe	9	260 × 180
E9-rt	88.4 ± 0.9	7 ± 11	193.0 ± 4.6	409 ± 24	C,O	8	290 × 290
E9-tp	85.5 ± 1.9	40 ± 15	172.8 ± 6.8	574 ± 34	O,C,Fe,S	16	430 × 200
F1-17	81.8 ± 1.0	90 ± 15	138.4 ± 3.5	965 ± 27	O,C,Si,Mg	4	375 × 290
F1-19	86.6 ± 2.9	30 ± 35	182.7 ± 8.8	488 ± 52	C,O,S,Fe	4	300 × 140
G2-rt	84.9 ± 1.1	50 ± 15	165.3 ± 5.4	646 ± 34	O,Si,C,Mg,Fe	4	230 × 140
G2-me	87.7 ± 1.6	15 ± 20	120.1 ± 3.4	1266 ± 30	O,C,Fe,Si,S	6	200 × 120
G3-tp	94.5 ± 3.1	−50 ± 35	164.7 ± 10.3	652 ± 69	O,C,Fe,S	3	300 × 280
G3-rt	84.5 ± 3.2	55 ± 40	137.5 ± 13.7	979 ± 120	O,C,Fe,Si	2	290 × 290
G3-bm	84.7 ± 2.2	50 ± 30	171.7 ± 9.2	584 ± 58	O,C,Fe,Mg,Si	3	270 × 200
G4	89.2 ± 2.2	−2 ± 25	155.5 ± 6.8	749 ± 47	O,C,Fe,Ni§	2	960 × 960§
G7-tp	93.3 ± 3.9	−45 ± 45	164.7 ± 10.2	652 ± 68	O, C, Fe	2	210 × 130
G9-tp	85.5 ± 1.9	40 ± 20	172.8 ± 6.8	574 ± 42	O,C,Si,Fe,Mg,S	2	870 × 430
G9-bm	89.3 ± 1.8	−3 ± 20	180.0 ± 9.4	511 ± 56	O,C,Fe,Si,Mg	3	850 × 550
G10-tp	85.7 ± 1.1	40 ± 15	180.6 ± 9.1	506 ± 54	O,C,Fe,Si	9	540 × 290
G10-bm	90.7 ± 3.2	−20 ± 35	180.1 ± 11.7	510 ± 71	O,C,Fe,Si,Mg	1	230 × 110
G11	83.7 ± 2.0	65 ± 25	170.5 ± 11.4	595 ± 74	O,C,Mg,Si,Fe,S	4	710 × 570
G12	88.2 ± 0.4	10 ± 5	176.0 ± 3.9	545 ± 23	C,O	65	800 × 430
Unclassified grains							
146	105.5 ± 2.2	−155 ± 20				–	200 × 160
21414	110.5 ± 1.9	−194 ± 20				–	275 × 200
21419	105.7 ± 1.8	−160 ± 15				–	235 × 235
51	114.8 ± 4.6	−225 ± 40				–	235 × 160

* Listed in order of decreasing abundance.
† Nanoglobules.
§ Includes coating and host Fe,C,Ni grain (see text for details); errors are 1σ.

4.2.2. Iron contents in ferromagnesian presolar silicates

Iron-bearing presolar silicate grains are abundant in all of the primitive chondrites studied to date (Fig. 14). The Fe contents of the presolar silicates in ALHA77307 span a range similar to those seen in other studies, including past work on ALHA77307 (Nguyen et al., 2010a), and are significantly higher than predicted from stellar observations and thermodynamic calculations. There are several possibilities that could account for the high Fe abundances and these have been discussed extensively in previous work (e.g., Floss and Stadermann, 2009a; Vollmer et al., 2009a; Nguyen et al., 2010a; Bose et al., 2010c). Here we provide a brief overview, with a particular emphasis on ALHA77307.

Equilibrium condensation calculations predict the initial formation of Mg-rich endmember silicates (e.g., Lodders and Fegley, 1999). Significant Fe can be incorporated as temperatures decrease, but diffusion is very slow at these lower temperatures (Palme and Fegley, 1990), and it is unlikely that chemical equilibrium can be maintained in the stellar environments in which these grains formed. Secondary alteration can also enhance Fe contents in presolar silicate grains. Incorporation of secondary Fe has been observed in the presolar silicates from the ungrouped carbonaceous chondrite Adelaide (Floss and Stadermann, 2012). Iron abundances in the Adelaide silicates span a range similar to those in Acfer 094 (Fig. 14); however, the median Fe content of the grains is a factor of two higher than that of the Acfer 094 presolar silicates, and they have much higher (Mg + Fe)/Si ratios than those in any of the other primitive chondrites. They also often exhibit Fe-rich rims that suggest an influx of Fe from the surrounding matrix (Floss and Stadermann, 2012). Adelaide is known to have experienced some thermal metamorphism (Brearley, 1991) and this process appears to have enhanced the Fe contents in these grains. In contrast, ALHA77307 is a pristine, highly unequilibrated CO chondrite, in which the matrix components are well-preserved (Brearley, 1993). The low abundances of Cr_2O_3 in its chondrule olivines indicate that it has escaped significant thermal metamorphism (Grossman and Brearley, 2005). ALHA77307 does contain some minor phyllosilicates and anhydrite that originated either on the

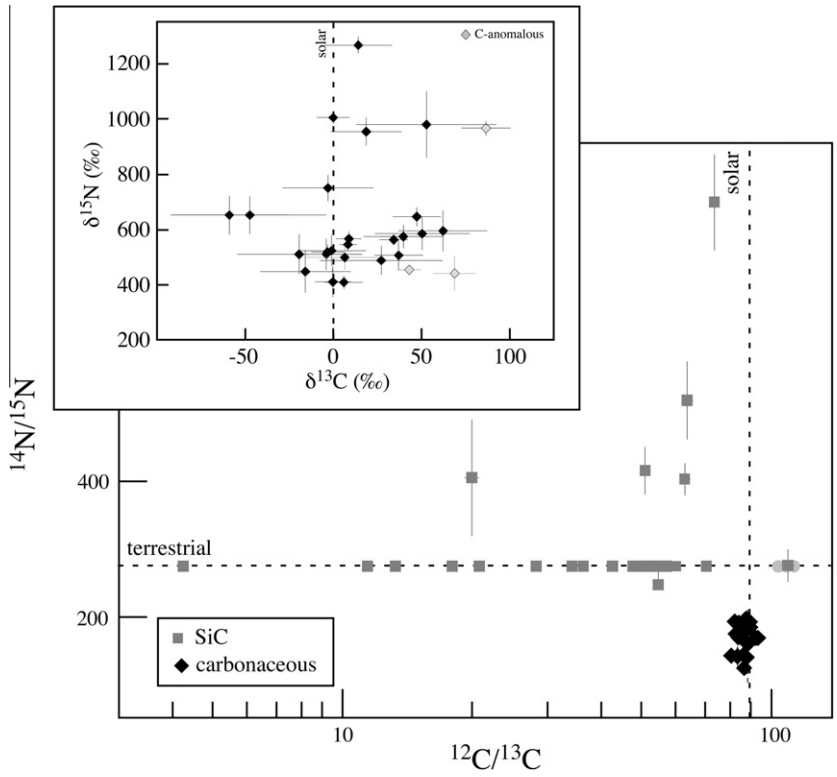

Fig. 9. Isotopic compositions of SiC and carbonaceous phases in ALHA77307. Grains that lack N isotopic data are arbitrarily plotted on the terrestrial N isotopic line. Gray circles show unidentified grains. The inset shows an expanded view of the carbonaceous grains [$\delta^{15}N = ((^{15}N/^{14}N)_{sample}/(^{15}N/^{14}N)_{standard}-1) \times 1000$. Errors are 1σ.

parent body (Scott and Krot, 2005) or as weathering products in Antarctica (Brearley, 1993). However, the degree of secondary aqueous alteration is minimal and occurred on a very localized scale (Brearley, 1993) and, thus cannot account for the widespread Fe enrichments observed in essentially all of the presolar silicates in ALHA77307.

Although equilibrium condensation cannot account for the high Fe contents of the presolar silicates in ALHA77307 and other primitive meteorites, modeling of grain growth indicates that significant Fe can be incorporated into major silicates such as olivine and pyroxene under non-equilibrium conditions (Gail and Sedlmayr, 1999; Ferrarotti and Gail, 2001). Gas-to-solid condensation experiments to produce silicate smokes have also shown that Fe-rich endmember oxides and silicates can be produced under kinetic conditions (Rietmeijer et al., 1999; Nuth et al., 2000). The stellar environments in which presolar silicates form are rapidly evolving and, thus, it seems likely that this process accounts for much of the Fe observed in these grains. Furthermore, although infrared spectra of the circumstellar envelopes around AGB stars suggest a predominance of Mg-rich silicates (e.g., Demyk et al., 2000), this may be at least partially due to the fact that Mg-rich features are more pronounced than warmer Fe-rich ones, and to the common practice of modeling such spectra using the laboratory spectra of olivines and pyroxenes with high Mg/Fe ratios (e.g., Dorschner et al., 1995; Fabian et al., 2000). A recent study successfully matched far-infrared spectral dust features of the star T Cep with Fe-rich silicates (Niyogi and Speck, 2010). This work, as well as the high Fe abundances observed in laboratory studies of presolar silicates, indicates that such models need to consider Fe-rich silicate dust analogs in order to better constrain the compositions of circumstellar dust grains.

Ultimately Fe isotopic measurements are required to determine if the Fe in presolar silicates is of primary or secondary origin, but only limited data exist to date. Several presolar grains from Acfer 094 do have non-solar Fe isotopic compositions, confirming a primary origin for the Fe in these grains (Mostefaoui and Hoppe, 2004; Floss et al., 2008; Vollmer and Hoppe, 2010; Ong et al., 2012). However, other presolar silicate grains have solar compositions within large errors (Vollmer and Hoppe, 2010; Bose et al., 2010c). These measurements are challenging due to the small sizes of the grains and the fact that they are typically surrounded by isotopically normal silicates. Additional measurements need to focus on particularly large grains or grains isolated from surrounding grains, for example by FIB milling (e.g., Nguyen et al., 2010b).

4.2.3. SiO_2

We identified three Group 1 SiO_2 grains (Fig. 3) in this study. Prior to our work, two other presolar SiO_2 grains, also both belonging to Group 1, were identified in MET 00426 and ALHA77307 (Floss and Stadermann, 2009a; Nguyen et al., 2010a). Thermodynamic calculations show that silica does not form under chemical equilibrium from

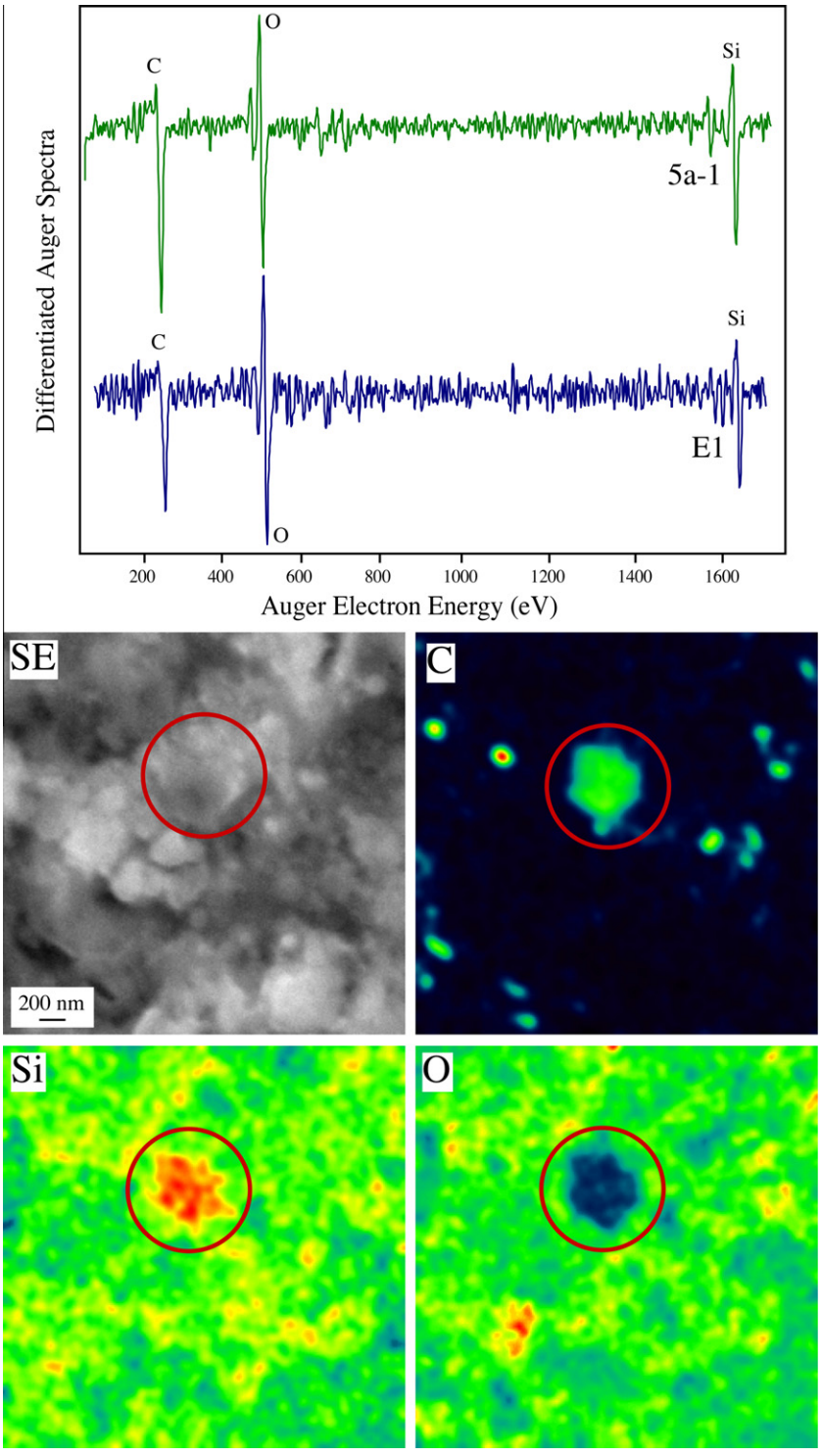

Fig. 10. Auger spectra for SiC grains 5a-1 and E1, and secondary electron and C, Si and O elemental images for SiC grain 5a-1.

a gas with standard elemental abundances, because the formation of Mg- and/or Fe-bearing silicates is thermodynamically more favorable (e.g. Gail and Sedlmayr, 1999). Silica may, however, condense in stellar winds under non-equilibrium conditions when only part of the gas phase SiO is consumed by the formation of Mg–Fe-silicates. This can occur in stars with low Mg/Si ratios and low mass-loss rates (Gail and Sedlmayr, 1999; Ferrarotti and Gail, 2001). In addition, Nagahara and Ozawa (2009) showed that the probability of silica condensation is enhanced in kinetically condensing systems of solar composition, and Rietmeijer et al. (2009) found that non-equilibrium condensation

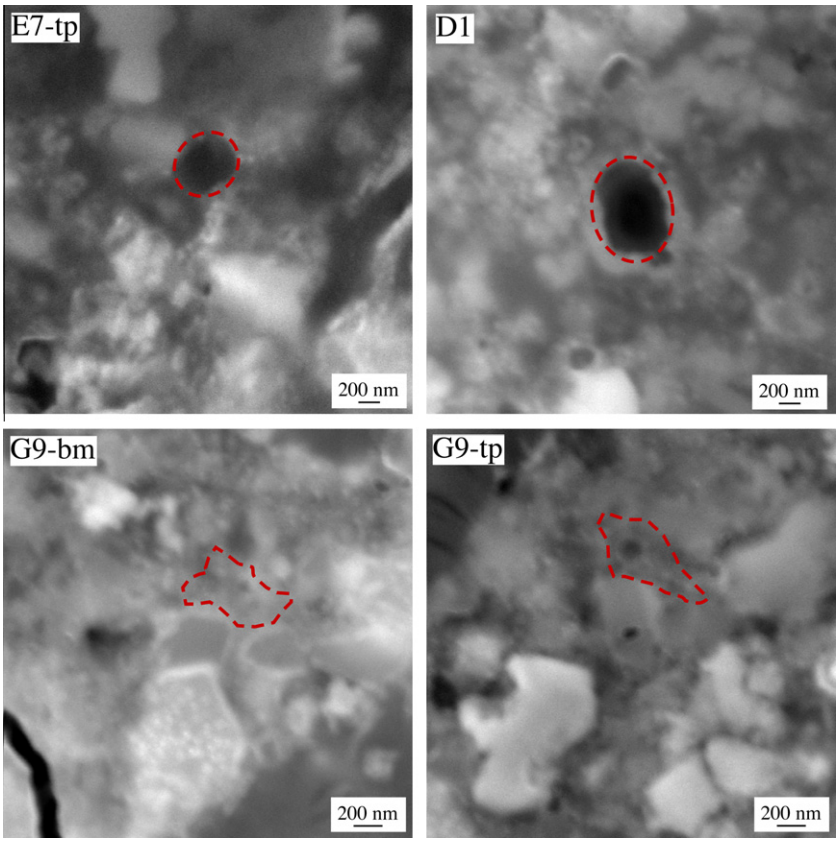

Fig. 11. Secondary electron images illustrating morphologies in the carbonaceous phases. E7-tp: smooth, platy; D1: nanoglobule; G9-bm and G9-tp: irregular.

experiments do produce silica aggregates, specifically the high-temperature polymorph tridymite.

Astronomical observations show the presence of a 13 μm feature in about half of all AGB stars, where it is predominantly associated with semi-regular (SR) variable stars and, to a lesser extent, Mira variable stars (e.g., Sloan et al., 1996). Attempts to constrain the phase responsible for the 13 μm feature indicate a variety of plausible contenders (e.g., Sloan et al., 1996, 2003; Fabian et al., 2001; Posch et al., 2003), including silica (Speck et al., 2000). There are arguments against SiO_2 as the carrier of the 13 μm feature, including opacity issues leading to reduced emission at the IR wavelengths, and the absence of a correlation between the 13 and ~10 μm silicate features in all stellar spectra (e.g., Fabian et al., 2001), and more than one carrier is probably responsible for this feature. However, if silica is indeed a product of non-equilibrium condensation, it may be a carrier in SR variable stars. These stars have lower mass-loss rates than Mira variable stars, leading to a lower gas density at the dust-forming radius (Ivezic and Knapp, 1999). At these lower densities, Si is less likely to react with other circumstellar species (e.g., MgO) to form magnesian silicates and, thus, may survive as SiO_2. Recently, spectra of BP Piscium, a first ascent giant star, were modeled by material that included crystalline sub-micrometer-sized cristobalite (Melis et al., 2010), another high-temperature polymorph of silica.

The TEM data for our SiO_2 grain indicate that it is amorphous. The grain may have condensed as an initially amorphous phase, or amorphization of an initially crystalline form of SiO_2 could have occurred as the grain traversed the interstellar medium. Although the data are limited, the experimental and observational data suggest that, if crystalline SiO_2 condenses in stellar environments, it may be more likely to do so as the high-temperature polymorphs tridymite or cristobalite than as quartz (DePew, 2006; Rietmeijer et al., 2009; Melis et al., 2010). However, more modeling efforts, as well as additional structural information on presolar SiO_2, are needed to provide definitive constraints.

4.2.4. Oxides

Three grains in our inventory have Al-oxide compositions (Table 2). Presolar Al-oxide grains are well-known from acid residues (e.g., Zinner, 2007) and have also been identified in meteorite thin sections (e.g., Floss and Stadermann, 2009a). Nearly all S-type AGB stars show broad emission features consistent with alumina dust (e.g., Sloan and Price, 1998). Under thermodynamic equilibrium, alumina is expected to condense at ~1500 K, well above the stability limit for silicates (Tielens et al., 1998). If the gas density has become too low for significant dust growth, a "freeze-out" of the condensation sequence occurs, and alumina remains the dominant dust component. Indeed, the ejecta of AGB stars with low mass-loss rates (10^{-9}–

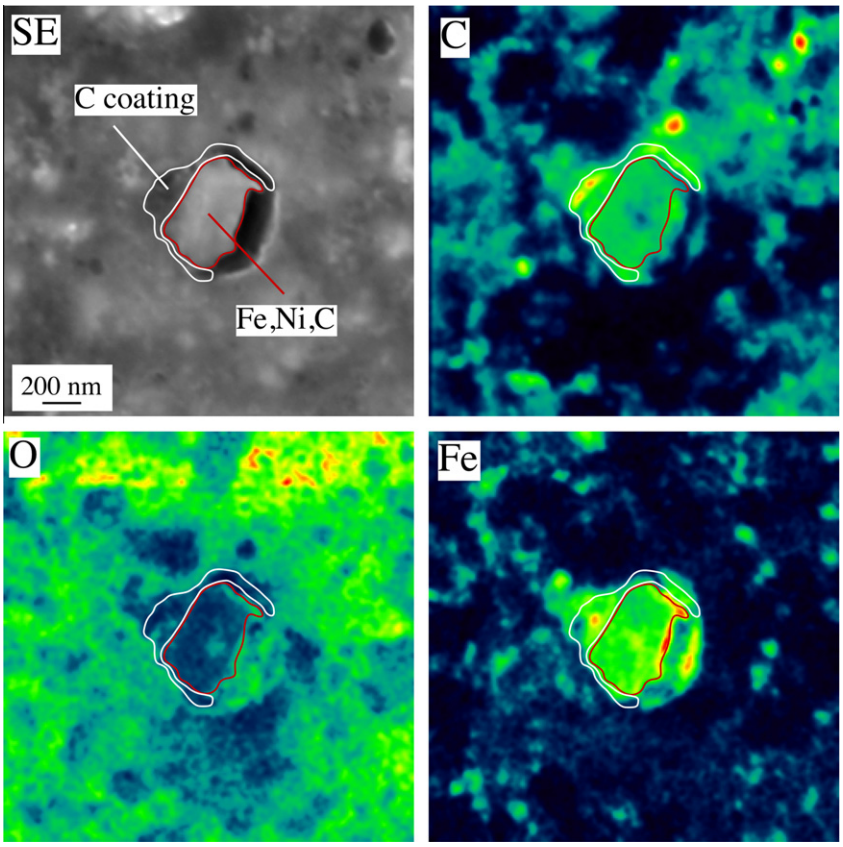

Fig. 12. Secondary electron and elemental distribution images of N-anomalous area G4 coating a host Fe,Ni,C grain (outlined in white and red, respectively). (For interpretation of the references to color in this figure legend, the reader is referred to the web version of this article.)

$10^{-7} M_{\odot}$ per year) contain significant fractions of alumina (Heras and Hony, 2005; Blommaert et al., 2006); this fraction decreases with increasing mass-loss rate, as observed in AGB stars in the Large Magellan Cloud (Dijkstra et al., 2005).

Our oxide grain inventory also includes two Fe-oxide grains and one Mg-oxide grain (Table 2). One of the Fe-oxide grains (21412) is stoichiometrically consistent with FeO (within 2σ errors), while the other one (54-7) is somewhat more O-rich. The Mg-oxide grain 55b-4 is stoichiometric MgO. Presolar FeO has previously been reported from Acfer 094 (Floss et al., 2008), but this is the first identification of presolar MgO. Both of the grains are approximately circular and have compact structures, in contrast to the aggregate structure exhibited by the FeO grain in Acfer 094 (Floss et al., 2008). FeO and MgO are the endmembers of the solid solution series magnesiowüstite ($Mg_xFe_{1-x}O$). As discussed in detail by Floss et al. (2008), magnesiowüstite can form under non-equilibrium conditions in Mg-rich AGB stars with low mass-loss rates ($dM/dt = 5 \times 10^{-6}$ per year; Ferrarotti and Gail, 2003). The Mg-rich endmember, MgO, forms first, but as temperatures drop, significant amounts of Fe can be incorporated. Magnesiowüstite has also been proposed as the carrier of the 19.5 μm emission feature observed in some AGB stars with low mass-loss rates that show little silicate emission (Posch et al., 2002); the best fit to the feature is obtained with an Fe-rich composition ($Mg_{0.1}Fe_{0.9}O$), similar to the FeO grains found in our study and in Acfer 094 (Floss et al., 2008).

Finally, one of our grains (33) is very Si-poor ($Si = 4.5 \pm 0.5$ at.%), with high abundances of Al (9 ± 2 at.%), and Fe (30 ± 3 at.%). The very low Si abundance suggests that this could be an oxide grain with minor Si contamination from the surrounding matrix. Unfortunately, no elemental map is available to evaluate this possibility. Regardless of whether the Si is a contaminant or intrinsic to the grain, its unusual composition indicates a complex formation history.

4.2.5. Composite grains

Grain 51-1 is an aggregate of two ferromagnesian silicate subgrains. Its O isotopic composition (Group 1) is homogeneous over both subgrains, but elemental compositions differ (Fig. 8). The bottom subgrain has an Fe + Mg/Si ratio consistent with olivine, while the other subgrain has a higher ratio (2.7 ± 0.4). Both subgrains are Fe-rich, but the Fe abundance is significantly higher in the top subgrain (Table 2). The high Fe content and elevated Fe + Mg/Si ratio of the top subgrain may argue for incorporation of secondary Fe into the grain (e.g., Floss and Stadermann, 2012). Secondary Fe could also be incorporated into the bottom subgrain, fortuitously elevating its Fe + Mg/Si ratio to a value consistent with olivine, which seems unlikely. However, it seems equally improbable that secondary alteration affected one

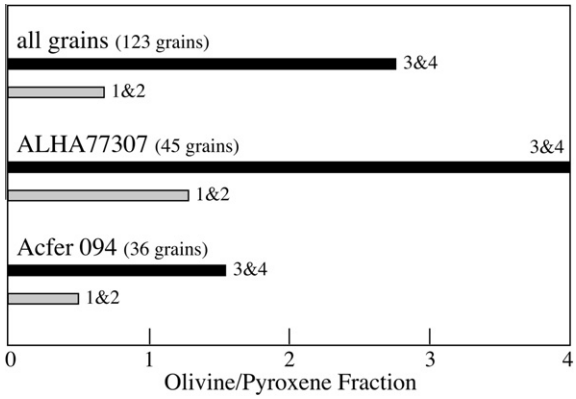

Fig. 13. Comparison of olivine/pyroxene fractions in presolar silicates from Groups 3 and 4 vs. 1 and 2. Data are shown for ALHA77307, Acfer 094 and the entire presolar silicate inventory (from the presolar grain database; http://presolar.wustl.edu/~pgd).

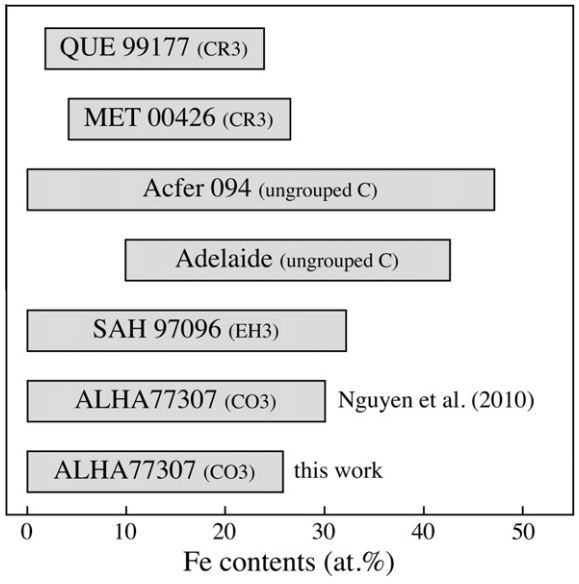

Fig. 14. Range of Fe contents in presolar silicate grains from ALHA77307 and other chondrites measured by Auger Nanoprobe. Data are from Bose et al. (2010c, 2010d), Floss and Stadermann (2009a, 2012), Nguyen et al. (2010a) and Vollmer et al. (2009a).

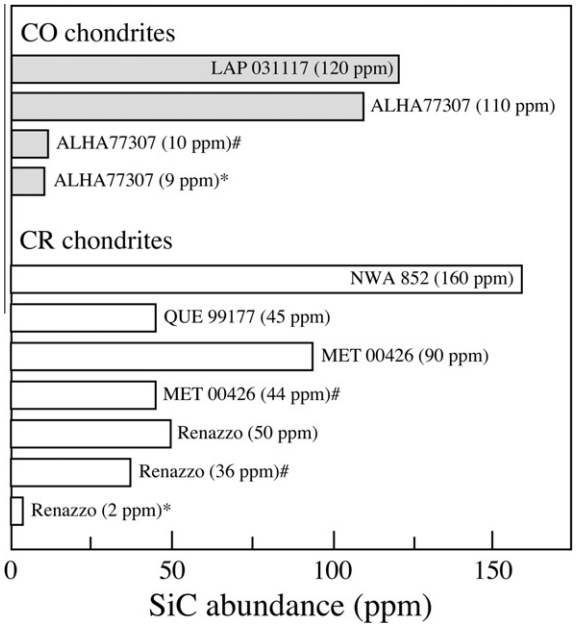

Fig. 15. SiC abundances in CO and CR chondrites; * from noble gas measurements; # from NanoSIMS imaging of IOM residues; others are NanoSIMS imaging of matrix material. Literature data are from Huss et al. (2003), Floss and Stadermann (2009b), Davidson et al. (2009), Leitner et al. (2010), and Haenecour and Floss (2011).

subgrain, but not the other. A more plausible alternative is that both subgrains formed under kinetic conditions from the same stellar source, but in somewhat different environments, resulting in slightly different elemental compositions.

The other composite grain, 51-8, contains several subgrains that vary in shape and size (50–100 nm; Fig. 7). The left portion of the grain (51-8-lt) has a pyroxene-like composition and contains some Ca, while the average composition of the aggregate subgrains on the right (51-8-rt) is non-stoichiometric, with a higher Fe abundance and higher Fe + Mg/Si ratio. The presence of Ca in the pyroxene-like subgrain may reflect condensation of a Ca-bearing phase and subsequent reaction with the gas at lower temperatures to form Ca-bearing pyroxene (e.g., Lodders and Fegley, 1999). The aggregate subgrains are compositionally intermediate between pyroxene and olivine (Table 2). Because this is an average composition obtained over several subgrains, we cannot distinguish whether all of the subgrains have the same homogeneous composition, or whether this composition reflects an average of subgrains with different individual compositions.

Finally, for both composite grains we note that the heterogeneity in elemental compositions, despite homogeneous O isotopic compositions, indicates a decoupling of isotopic and elemental compositions in the stellar environments where these grains formed.

4.3. SiC grains

All but two of the SiC grains identified in ALHA77307 can be classified as mainstream SiC of AGB origin, with $^{12}C/^{13}C$ ratios between 21 and 75 (Table 3). Note that some of these could be X or Z grains that we cannot distinguish because we lack data for other diagnostic isotopic systems; however, the majority are probably mainstream grains because these dominate the SiC population (Zinner, 2007). One grain has a $^{12}C/^{13}C$ ratio of ~4 and is most likely an A + B grain; J-type C stars and born-again AGB stars are possible stellar sources of these grains (Amari et al., 2001). Finally, one grain with a $^{12}C/^{13}C$ ratios of >100 may be a Y grain. However, most Y grains have high $^{14}N/^{15}N$ ratios, in contrast to the normal N isotopic composition of our grain (Table 3) and, therefore, its classification is tentative.

The abundance of SiC grains in ALHA77307 (~110 ppm) is shown in Fig. 15, along with other estimates from CO3 chondrites, as well as several CR chondrites. The abundances shown are based on three different approaches: noble gas measurements of acid residues (Huss et al., 2003), NanoSIMS ion imaging measurements matrix areas in thin sections (Floss and Stadermann, 2009b; Leitner et al., 2010; Haenecour and Floss, 2011; this study) and ion imaging of IOM separates extracted from bulk meteorites (Davidson et al., 2009). For the CR chondrites, all of the data indicate that SiC abundances determined by ion imaging measurements (whether in thin section matrix areas or IOM separates) are significantly higher than the estimate based on noble gas data (25–160 ppm vs. ~2 ppm). Davidson et al. (2009) noted that SiC abundances were similar in all the CR chondrites they analyzed (ranging from CR1 to CR3), indicating that aqueous alteration does not play a significant role in destroying SiC grains. They suggested that the discrepancy between the noble gas and NanoSIMS measurements could be due to loss of noble gases or destruction of a small gas-rich fraction of SiC, perhaps during the chemical separation procedure.

For the CO chondrites, the SiC abundances based on ion imaging of matrix material, are also much higher than the noble gas estimate (Fig. 15), providing additional evidence that the chemical separation procedures give only lower limits to SiC abundances. However, in contrast to the data for CR chondrites, ion imaging of ALHA77307 IOM separates (Davidson et al., 2009) also shows a low abundance of SiC, similar to the abundance estimate from the noble gas data. The reason for this discrepancy is presently unclear. Sample preparation and/or analytical differences are one possibility, but this seems unlikely since a similar discrepancy does not exist for the CR chondrites. Similarly, attribution to poor statistics seems unlikely since the ranges in area analyzed (23,800 μm^2 in this study, 11,050 μm^2 by Haenecour and Floss, 2011, and 7683 μm^2 by Davidson et al., 2009) are comparable to or higher than those of the CR chondrites. Sample heterogeneity could account for the difference as it has been observed that presolar silicate grains are not uniformly distributed in different matrix areas (e.g., Floss and Stadermann, 2009a; Vollmer et al., 2009a), and our ion imaging studies naturally focus on areas that we have identified as having high presolar grain concentrations. However, it seems unusual that such a bias would be evident in work on the CO chondrites, but not the CR chondrites.

4.4. Carbonaceous grains

4.4.1. Compositions and morphologies

Nitrogen isotopic anomalies are present in the matrix of ALHA77307 as discrete hotspots with large ^{15}N enrichments ($\delta^{15}N$ up to ~1265‰). Three of these hotspots (D1, E7-tp and F1-17) also exhibit ^{13}C excesses (Fig. 9; Table 4). These hotspots consist of carbonaceous matter and are similar in morphology, elemental make-up and isotopic compositions to the organic N-anomalous matter observed in IDPs and in other primitive meteorites (e.g., Floss et al., 2006, 2010, 2011; Busemann et al., 2006, 2009; Floss and Stadermann, 2009b; Zega et al., 2010). In a study of the N isotopic compositions of D-rich IDPs, Aléon et al. (2003) determined N concentrations based on CN^-/C^- ratios calibrated to a variety of organic phases with known N concentrations. Although calibration curves based on measurements made with other SIMS instruments are not strictly appropriate for determining the N concentrations using CN^-/C^- ratios from our NanoSIMS measurements, we have used the calibration curve of Aléon et al. (2003) to provide a first-order estimate of the N abundances in our hotspots. The CN^-/C^- ratios in the ALHA77307 hotspots correspond to N concentrations of less than 5 wt.%; this is in good agreement with our Auger data, which show that N abundances are below detection limits (estimated to be on the order of 3 at.%) in almost all of these hotspots.

High-resolution images in the Auger Nanoprobe indicate that three of our ^{15}N-rich hotspots are circular in shape and may be hollow (e.g., Fig. 11), like the nanoglobules seen in many carbonaceous chondrites (Nakamura-Messenger et al., 2006; Garvie et al., 2008), ordinary chondrites (Cody et al., 2011) and cometary samples (De Gregorio et al., 2010). In addition, two of them exhibit ^{13}C and ^{15}N excesses (Table 4), like the nanoglobule found by Floss and Stadermann (2009b) in the MET 00426 CR3 chondrite. There is currently no consensus on the origin of nanoglobules and both parent body and interstellar processes have been invoked (e.g., Cody and Alexander, 2005; Nakamura-Messenger et al., 2006; De Gregorio et al., 2010). Moreover, there does not appear to be a clear distinction between nanoglobules and other more irregular carbonaceous grains in terms of isotopic and elemental compositions. Floss et al. (2011) observed that hotspots with C and/or N isotopic anomalies all consist of amorphous carbonaceous matter, but with variable morphologies that include nanoglobules, blocky grains and aggregates of grains.

Finally, ^{15}N-enriched organic matter is present as a coating around an Fe,Ni,C grain that is not isotopically anomalous (Fig. 12). Surface coatings have been observed around pristine presolar SiC grains (Bernatowicz et al., 2003; Croat et al., 2009); C and N imaging of one such surface coating on a ^{15}N-depleted SiC grain was enriched in ^{15}N, suggesting a protosolar or interstellar origin for the coating. A similar origin may account for the ^{15}N-rich coating observed in this study.

4.4.2. Sources of isotopic anomalies

Most of the N isotopic anomalies present in the organic matter of IDPs and primitive meteorites is ^{15}N-enriched, but depletions in ^{15}N are also sometimes observed (e.g., Floss and Stadermann, 2009c). These anomalies have typically been attributed to chemical fractionation via ion–molecule exchange reactions in dense cold molecular clouds or in the protosolar nebula (Charnley and Rodgers, 2002; Rodgers and Charnley, 2008). They may also be produced in the outer regions of the solar nebula via molecular depletion from the gas phase onto surfaces of dust grains (Terzieva and Herbst, 2000; Aléon and Robert, 2004; Aléon, 2010). The large variations observed in the $\delta^{15}N$ values could be due to variable fractionation effects for different types of N-bearing molecules (e.g., Sandford et al., 2001)

or to the particular chemical reactions that produce a given organic molecule. In addition, secondary processing may also have an effect on N isotopic compositions.

Correlated C and N isotopic anomalies are observed in three carbonaceous grains from ALHA77307. Similar grains have been found in IDPs and other meteorites, although they are far less common than grains that exhibit only N isotopic anomalies (Floss et al., 2006, 2010; Floss and Stadermann, 2009b). In most cases these grains exhibit ^{13}C depletions, but ^{13}C enrichments have also been found. Chemical fractionation of C isotopes can occur in cold and dense molecular clouds by multiple gas-phase reactions (e.g., Langer et al., 1984), with different reaction pathways resulting in different fractionations; CO self-shielding in the protosolar nebula has also been suggested as a way to fractionate C (Hashizume et al., 2011). It has been proposed that the Sun is depleted in ^{13}C by $\sim$100‰ (Hashizume et al., 2004), suggesting a possible solar nebula origin for some of these C isotopic anomalies. However, we note that ^{13}C depletions up to 340‰ have been observed in carbonaceous matter from the CR3 chondrites QUE 99177 and MET 00426 (Floss and Stadermann, 2009b), indicating that additional fractionation processes are still required to account for the C isotopic compositions of much of the meteoritic organic matter.

The presence of N isotopic anomalies in ALHA77307 with magnitudes similar to those observed in primitive IDPs and meteorites indicates that ALHA77307 has preserved primitive organic matter. However, unlike other primitive meteorites whose IOM exhibits bulk N isotopic anomalies (e.g., the CR chondrites, Bells, Tagish Lake), the bulk N isotopic composition of macromolecular organic matter in ALHA77307 is isotopically normal (Alexander et al., 2007). In addition, ALHA77307 does not exhibit the larger, more diffuse ^{15}N-enriched regions that are commonly seen in the CR chondrites and some IDPs (Floss et al., 2006; Busemann et al., 2006, 2009; Floss and Stadermann, 2009b). Busemann et al., (2007) argued that the absence of bulk N isotopic anomalies in the organic matter from most meteorite groups, compared to the CR chondrites, reflects the loss of a very fragile carrier of the ^{15}N enrichments. Several Raman parameters do suggest that the IOM in ALHA77307 has experienced more thermal processing than IOM in the CR chondrites, leading to less disorder and increased aromatic domain size (Busemann et al., 2007; Bonal et al., 2007). However, secondary processing has clearly not been so pervasive as to lead to the complete destruction of N isotopic anomalies in this meteorite. Moreover, the high abundance of presolar silicates in ALHA77307 is a clear indication that the degree of thermal metamorphism was limited; presolar grain abundances and elemental compositions are similar in ALHA77307 and the CR3 chondrites (Floss and Stadermann, 2009a; Nguyen et al., 2010a). Indeed, the peak metamorphic temperature experienced by ALHA77307 is similar to that of the CR chondrites, about 200 °C (Huss et al., 2006).

A comparison of ALHA77307 with the ungrouped carbonaceous chondrite Adelaide, which shows a number of affinities to the CO chondrites (Brearley, 1991), indicates that the IOM in Adelaide is very similar to ALHA77307 IOM, from which Busemann et al. (2007) concluded that Adelaide had not experienced much thermal metamorphism. However, a study of presolar silicate and oxide grains in Adelaide (Floss and Stadermann, 2012) shows that this meteorite is more thermally processed than ALHA77307, with lower abundances of presolar grains and evidence for secondary enhancement of Fe contents in the presolar silicates. The matrix of Adelaide is also more crystalline and has fewer amorphous silicates than ALHA77307, providing additional evidence of thermal annealing (Brearley, 1991). These discrepancies suggest a decoupling between the effect of thermal metamorphism on IOM and its effect on matrix silicates. An alternative possibility is that the IOM present in primitive extraterrestrial materials originated from multiple reservoirs with distinct N isotopic compositions (e.g., Floss et al., 2012).

5. CONCLUSIONS

The circumstellar grain population in ALHA77307 is dominated by materials formed in C- and O-rich outflows from AGB stars (>80%), with moderate (<10%) contributions from SNe. One grain has a very high $^{17}O/^{16}O$ ratio that is incompatible with dredge-up processes in low-mass AGB stars; nova origins have previously been suggested for such grains, but new models indicate large discrepancies with the grain data (Gyngard et al., 2011). Rare grains of phases such as SiO_2, FeO and MgO are present in the presolar grain inventory of ALHA77307, but the majority of the O-anomalous grains are ferromagnesian silicates with elemental compositions similar to those observed in other studies. Silicates with olivine compositions are overabundant among Group 4 grains compared to grains from Groups 1 and 2. If grain compositions are significantly altered by irradiation and sputtering as they traverse the interstellar medium, resulting in lower olivine/pyroxene ratios, the difference could reflect injection of presolar material with high olivine abundances from a nearby supernova in the early solar nebula, with accretion into parent bodies before the grain compositions are altered by secondary processes.

ALHA77307 also contains carbonaceous grains with N isotopic anomalies and occasional C isotopic anomalies similar to those found in primitive IDPs and other meteorites. However, unlike the CR chondrites, which have IOM with bulk ^{15}N enrichments, the organic matter in ALHA77307 has a terrestrial bulk N isotopic composition. Thermal annealing with loss of a ^{15}N carrier could account for the difference. However, presolar grain abundances and elemental compositions indicate that ALHA77307 is as primitive as the CR3 chondrites QUE 99177 and MET 00426, suggesting a decoupling of the effects of thermal metamorphism on IOM and matrix silicates.

ACKNOWLEDGEMENTS

We thank Tim Smolar and Eric Inazaki for maintenance of the NanoSIMS 50 and PHI 700 Auger Nanoprobe. We would also like to thank two anonymous reviewers and Dr. Jérôme Aléon for extensive comments. This work was supported by NASA grants

NNX07AU8OH (M. Bose), and NNX10AI64G and NNX10AH43G (C. Floss).

REFERENCES

Aléon J. (2010) Multiple origins of nitrogen isotopic anomalies in meteorites and comets. *Astrophys. J.* **722**, 1342–1351.

Aléon J. and Robert F. (2004) Interstellar chemistry recorded by nitrogen isotopes in solar system organic matter. *Icarus* **167**, 424–430.

Aléon J., Robert F., Chaussidon M. and Marty B. (2003) Nitrogen isotopic composition of macromolecular organic matter in interplanetary dust particles. *Geochim. Cosmochim. Acta* **67**, 3773–3783.

Alexander C. M. O'D., Fogel M., Yabuta H. and Cody G. D. (2007) The origin and evolution of chondrites recorded in the elemental and isotopic compositions of their organic matter. *Geochim. Cosmochim. Acta* **71**, 4380–4403.

Amari S., Nittler L. R., Zinner E., Lodders K. and Lewis R. S. (2001) Presolar SiC grains of type A and B: their isotopic compositions and stellar origins. *Astrophys. J.* **559**, 463–483.

Bernatowicz T., Messenger S., Pravdivtseva O. V., Swan P. and Walker R. M. (2003) Pristine presolar silicon carbide. *Geochim. Cosmochim. Acta* **67**, 4679–4691.

Blommaert J. A. D. L., Groenewegen M. A. T., Okumura K., Ganesh S., Omont A., Cami J., Glass I. S., Habing H. J., Schultheis M., Simon G. and van Loon J. Th. (2006) ISO mid-infrared spectroscopy of galactic bulge AGB stars. *Astron. Astrophys.* **460**, 555–563.

Bonal L., Bourot-Denise M., Quirico E., Montagnac G. and Lewin E. (2007) Organic matter and metamorphic history of CO chondrites. *Geochim. Cosmochim. Acta* **71**, 1605–1623.

Bose M., Floss C. and Stadermann F. J. (2009) Presolar silicate and oxide dust in ALHA77307. *Meteorit. Planet. Sci.* **44**, A36 (abstr.).

Bose M., Floss C., Stadermann F. J., Stroud R. M., and Speck A. K. (2010a) The origin of presolar silica grains in AGB Stars. *Lunar Planet. Sci. XLI*. Lunar Planet. Inst., Houston. #1812 (abstr.).

Bose M., Floss C. and Stadermann F. J. (2010b) Nitrogen isotopic anomalies in ALHA77307. *Meteorit. Planet. Sci.* **45**, A19 (abstr.).

Bose M., Floss C. and Stadermann F. J. (2010c) An investigation into the origin of Fe-rich presolar silicates in Acfer 094. *Astrophys. J.* **714**, 1624–1636.

Bose M., Zhao X., Floss C., Stadermann F. J. and Lin Y. (2010d) Stardust material in the paired enstatite meteorites: SAH 97096 and SAH 97159. *Proc. Symp. Nuclei Cosmos XI*, 138.

Bose M., Floss C. and Stadermann F. J. (2011a) Carbonaceous N-anomalous grains in the CO3.0 meteorite ALHA77307. *Lunar Planet. Sci. XLII*, Lunar Planet. Inst., Houston. #1444.

Bose M., Floss C. and Stadermann F. J. (2011b) Non-equilibrium presolar condensates in primitive meteorites. *Meteorit. Planet. Sci.* **46**, A26 (abstr.).

Brearley A. (1991) Adelaide: matrix chemistry and mineralogy. *Lunar Planet. Sci. XXII*, Lunar Planet. Inst., Houston. pp. 133–134 (abstr.).

Brearley A. J. (1993) Matrix and fine-grained rims in the unequilibrated CO3 chondrite, ALHA77307 – origins and evidence for diverse, primitive nebular dust components. *Geochim. Cosmochim. Acta* **57**, 1521–1550.

Busemann H., Young A. F., Alexander C. M. O'D., Hoppe P., Mukhopadhyay S. and Nittler L. R. (2006) Interstellar chemistry recorded in organic matter from primitive meteorites. *Science* **312**, 727–730.

Busemann H., Alexander C. M. O'D. and Nittler L. R. (2007) Characterization of insoluble organic matter in primitive meteorites by microRaman spectroscopy. *Meteorit. Planet. Sci.* **42**, 1387–1416.

Busemann H., Nguyen A. N., Cody G. D., Hoppe P., Kilcoyne A. L. D., Stroud R. M., Zega T. J. and Nittler L. R. (2009) Ultra-primitive interplanetary dust particles from the comet 26P/Grigg-Skjellerup dust stream collection. *Earth Planet. Sci. Lett.* **288**, 44–57.

Carrez P., Demyk K., Cordier P., Gengembre L., Grimblot J., D'Hendecourt L., Jones A. P. and Leroux H. (2002) Low-energy helium ion irradiation-induced amorphization and chemical changes in olivine: insights for silicate dust evolution in the interstellar medium. *Meteorit. Planet. Sci.* **37**, 1599–1614.

Charnley S. B. and Rodgers S. D. (2002) The end of interstellar chemistry as the origin of nitrogen in comets and meteorites. *Astrophys. J.* **569**, L133–L137.

Cody G. and Alexander C. M. O'D. (2005) NMR studies of chemical structural variation of insoluble organic matter from different carbonaceous chondrite groups. *Geochim. Cosmochim. Acta* **69**, 1085–1097.

Cody G. D., Heying E., Alexander C. M. O'D., Nittler L. R., Kilcoyne A. L. D., Sandford S. A. and Stroud R. M. (2011) Establishing a molecular relationship between chondritic and cometary organic solids. *Proc. Natl. Acad. Sci.*, doi:10.1073/pnas.1015913108.

Crozaz G., Floss C. and Wadhwa M. (2003) Chemical alteration and REE mobilization in meteorites from hot and cold deserts. *Geochim Cosmochim. Acta* **67**, 4727–4741.

Croat T. K., Bernatowicz T. J. and Stadermann F. J. (2009) Auger and NanoSIMS investigations of pristine presolar SiC surfaces. *Lunar Planet. Sci. XL*. Lunar Planet. Inst., Houston. #1887 (abstr.).

Davidson J., Busemann H., Alexander C. M. O'D., Nittler L. R., Schrader D. L., Orthous-Daunay F. R., Quirico E., Franchi I. A. and Grady M. M. (2009) Presolar SiC abundances in primitive meteorites by NanoSIMS raster ion imaging of insoluble organic matter. *Lunar Planet. Sci. XL*. Lunar Planet. Inst., Houston. #1853 (abstr.).

De Gregorio B. T., Stroud R. M., Nittler L. R., Alexander C. M. O'D., Kilcoyne A. L. D. and Zega T. J. (2010) Isotopic anomalies in organic nanoglobules from comet 81P/Wild 2: comparison to Murchison nanoglobules and isotopic anomalies induced in terrestrial organics by electron irradiation. *Geochim. Cosmochim. Acta* **74**, 4454–4470.

Demyk K., Dartois E., Wiesemeyer H., Jones A. and d'Hendecourt L. (2000) Composition of the silicate dust around OH/IR stars. *Astron. Astrophys.* **364**, 170–178.

Demyk K., Carrez Ph., Leroux H., Cordier P., Jones A. P., Borg J., Quirico E., Raynal P. I. and d'Hendecourt L. (2001) Structural and chemical alteration of crystalline olivine under low energy He+ irradiation. *Astron. Astrophys.* **368**, L38–L41.

DePew K. D. (2006) On the astromineralogy of the 13 μm feature in the spectra of oxygen-rich AGB stars. **M.S**. Thesis, University of Missouri, 94 pp.

Dijkstra C., Speck A. K., Reid R. B. and Abraham P. (2005) The 10 μm feature of M-Type stars in the Large Magellanic Cloud and the dust condensation sequence. *Astrophys. J.* **633**, L133–L136.

Dorschner J., Begemann B., Henning Th., Jäger C. and Mutschke H. (1995) Steps toward interstellar silicate mineralogy II. Study of Mg-Fe-silicate glasses of variable composition. *Astron. Astrophys.* **300**, 503–520.

Fabian D., Jäger C., Henning Th., Dorschner J. and Mutschke H. (2000) Steps toward interstellar silicate mineralogy V. Thermal

evolution of amorphous magnesium silicates and silica. *Astron. Astrophys.* **364**, 282–292.

Fabian D., Posch Th., Mutschke H., Kerschbaum F. and Dorschner J. (2001) Infrared optical properties of spinels. A study of the carrier of the 13, 17 and 32 μm emission features observed in ISO-SWS spectra of oxygen-rich AGB stars. *Astron. Astrophys.* **373**, 1125–1138.

Ferrarotti A. S. and Gail H.-P. (2001) Mineral formation in stellar winds. II. Effects of Mg/Si abundance variations on dust composition in AGB stars. *Astron. Astrophys.* **371**, 133–151.

Ferrarotti A. S. and Gail H.-P. (2003) Mineral formation in stellar winds. IV. Formation of magnesiowüstite. *Astron. Astrophys.* **398**, 1029–1039.

Floss C. and Stadermann F. J. (2009a) Auger Nanoprobe analysis of presolar ferromagnesian silicate grains from primitive CR chondrites QUE 99177 and MET 00426. *Geochim. Cosmochim. Acta* **73**, 2415–2440.

Floss C. and Stadermann F. J. (2009b) High abundances of circumstellar and interstellar C-anomalous phases in the primitive CR3 chondrites QUE 99177 and MET 00426. *Astrophys. J.* **697**, 1242–1255.

Floss C. and Stadermann F. J. (2009c) Interstellar components in the primitive CR3 chondrites QUE 99177 and MET 00426. *Lunar Planet. Sci. XL.* Lunar Planet. Inst., Houston. #1083 (abstr.).

Floss C. and Stadermann F. J. (2012) Presolar silicate and oxide abundances and compositions in the ungrouped carbonaceous chondrite Adelaide and the K chondrite Kakangari: the effects of secondary processing. *Meteorit. Planet. Sci.* **47**, 992–1009.

Floss C., Stadermann F. J., Bradley J. P., Dai Z. R., Bajt S., Graham G. and Lea A. S. (2006) Identification of isotopically primitive interplanetary dust particles: a NanoSIMS isotopic imaging study. *Geochim. Cosmochim. Acta* **70**, 2371–2399.

Floss C., Stadermann F. J. and Bose M. (2008) Circumstellar Fe oxide from the Acfer 094 carbonaceous chondrite. *Astrophys. J.* **672**, 1266–1271.

Floss C., Stadermann F. J., Mertz A. F. and Bernatowicz T. J. (2010) A NanoSIMS and Auger Nanoprobe investigation of an isotopically primitive interplanetary dust particle from the 55P/Tempel-Tuttle targeted stratospheric dust collector. *Meteorit. Planet. Sci.* **45**, 1889–1905.

Floss C., Le Guillou C., Stadermann F. J. and Brearley A. J. (2011) Coordinated NanoSIMS and TEM analyses of C- and N-anomalous phases in the CR3 chondrite MET 00426. *Lunar Planet. Sci. XLII.* Lunar Planet. Inst., Houston. #1455 (abstr.).

Floss C., Noguchi T. and Yada T. (2012) Ultracarbonaceous Antarctic micrometeorites: origins and relationships to other primitive extraterrestrial materials. *Lunar Planet. Sci. XLIII.* Lunar Planet. Inst., Houston. #1217 (abstr.).

Gail H.-P. and Sedlmayr E. (1999) Mineral formation in stellar winds. I. Condensation sequence of silicate and iron grains in stationary oxygen rich outflows. *Astron. Astrophys.* **347**, 594–616.

Gail H.-P., Zhukovska S. V., Hoppe P. and Trieloff M. (2009) Stardust from asymptotic giant branch stars. *Astrophys. J.* **698**, 1136–1154.

Garvie L. A. J., Baumgardner G. and Buseck P. R. (2008) Scanning electron microscopical and cross sectional analysis of extraterrestrial carbonaceous nanoglobules. *Meteorit. Planet. Sci.* **43**, 899–903.

Grossman J. N. and Brearley A. J. (2005) The onset of metamorphism in ordinary and carbonaceous chondrites. *Meteorit. Planet. Sci.* **40**, 87–122.

Gyngard F., Nittler L. R., Zinner E. and José J. (2010a) Oxygen-rich stardust grains from novae. *Proc. Symp. Nuclei Cosmos XI*, 141.

Gyngard F., Zinner E., Nittler L. R., Morgand A., Stadermann F. J. and Hynes K. M. (2010b) Automated NanoSIMS measurements of spinel stardust from the Murray meteorite. *Astrophys. J.* **717**, 107–120.

Gyngard F., Nittler L. R., Zinner E., José J. and Cristallo S. (2011) New reaction rates and implications for nova nucleosynthesis and presolar grains. *Lunar Planet. Sci. XL.* Lunar Planet. Inst., Houston. #2675 (abstr.).

Haenecour P. and Floss C. (2011) High abundance of stardust in the CO3.0 chondrite LaPaz 031117. *Meteorit. Planet. Sci.* **46**, A85 (abstr.).

Hashizume K., Chaussidon M., Marty B. and Terada K. (2004) Protosolar carbon isotopic composition: implications for the origin of meteoritic organics. *Astrophys. J.* **600**, 480–484.

Hashizume K., Takahata N., Naraoka H. and Sano Y. (2011) Extreme oxygen isotope anomaly with a solar origin detected in meteoritic organics. *Nat. Geosci.* **4**, 165–168.

Heras A. M. and Hony S. (2005) Oxygen-rich AGB stars with optically thin dust envelopes. *Astron. Astrophys.* **439**, 171–182.

Huss G., Meshik A. P., Smith J. B. and Hohenberg C. (2003) Presolar diamond, silicon carbide, and graphite in carbonaceous chondrites: implications for thermal processing in the solar nebula. *Geochim. Cosmochim. Acta* **67**, 4823–4848.

Huss G. R., Rubin A. E. and Grossman J. N. (2006) Thermal metamorphism in chondrites. In *Meteorit. Early Sol. Sys. II* (eds. D. S. Lauretta and , Jr.H. Y. McSween). University of Arizona Press, Tucson, pp. 567–586.

Ivezic Z. and Knapp G. R. (1999) Link between mass-loss and variability type for AGB stars? In *Asymptotic Giant Branch Stars* (eds. T. Le Bertre, A. Lebre and C. Waelkens). IAU Symposium No. 191. Astronomical Society of the Pacific, San Francisco.pp. 395-400.

José J., Hernanz M., Amari S., Lodders K. and Zinner E. (2004) The imprint of nova nucleosynthesis in presolar grains. *Astrophys. J.* **612**, 414–428.

Keller L. P. and Messenger S. (2011) On the origins of GEMS grains. *Geochim. Cosmochim. Acta.* **75**, 5336–5365.

Kemper F., Waters L. B. F. M., de Koter A. and Tielens A. G. G. M. (2001) Crystallinity versus mass-loss rate in asymptotic giant branch stars. *Astron. Astrophys.* **369**, 132–141.

Langer W. D., Graedel T. E., Frerking M. A. and Armentrout P. B. (1984) Carbon and oxygen isotope fractionation in dense interstellar clouds. *Astrophys. J.* **277**, 581–590.

Leitner J., Hoppe P., Vollmer C. and Zipfel J. (2010) The inventory of presolar grains in primitive meteorites: a NanoSIMS study of C-, N-, and O-isotopes in NWA 852. *Proc. Symp. Nuclei Cosmos XI*, 144.

Lodders K. and Fegley B. (1999) Condensation chemistry of circumstellar grains. In *Asymptotic Giant Branch Stars* (eds. T. Le Bertre, A. Lebre and C. Waelkens). IAU Symposium No. 191. Astronomical Society of the Pacific. San Francisco. pp. 279-289.

Melis C., Gielen C., Chen C. H., Rhee J. H., Song I. and Zuckerman B. (2010) Shocks and a giant planet in the disk orbiting BP Piscium? *Astrophys. J.* **724**, 470–479.

Min M., Waters L. B. F. M., de Koter A., Hovenier J. W., Keller L. P. and Markwick-Kemper F. (2007) The shape and composition of interstellar silicate grains. *Astron. Astrophys.* **462**, 667–676.

Mostefaoui S. and Hoppe P. (2004) Discovery of abundant in situ silicate and spinel grains from red giant stars in a primitive meteorite. *Astrophys. J.* **613**, L149–L152.

Nagahara H. and Ozawa K. (2009) Condensation kinetics of forsterite and metal and chemical fractionation in the protosolar nebula. *Lunar Planet. Sci. XL.* Lunar Planet. Inst., Houston. #2158 (abstr.).

Nakamura-Messenger K., Messenger S., Keller L. P., Clemett S. J. and Zolensky M. E. (2006) Organic globules in the Tagish Lake meteorite: remnants of the protosolar disk. *Science* **314**, 1439–1442.

Nguyen A. N., Stadermann F. J., Zinner E., Stroud R. M., Alexander C. M. O'D. and Nittler L. R. (2007) Characterization of presolar silicate and oxide grains in primitive carbonaceous chondrites. *Astrophys. J.* **656**, 1223–1240.

Nguyen A. N., Nittler L. R., Stadermann F. J., Stroud R. M. and Alexander C. M. O'D. (2010a) Coordinated analyses of presolar grains in the Allan Hills 77307 and Queen Elizabeth Range 99177 meteorites. *Astrophys. J.* **719**, 166–189.

Nguyen A. N., Messenger S., Ito M., and Rahman Z. (2010b) Mg isotopic measurement of FIB-isolated presolar silicate grains. *Lunar Planet. Sci. XLI*. Lunar Planet. Inst., Houston. #2413 (abstr.).

Niyogi S. G. and Speck A. K. (2010) A temporal study of O-rich pulsating variable AGB star, T Cep: investigation on dust formation, mineralogy and morphology of dust grains. *Am. Astron. Soc*. **42**, #215 (abstr.).

Nittler L. R. and Hoppe P. (2005) Are presolar silicon carbide grains from novae actually from supernovae? *Astrophys. J.* **631**, L89–L92.

Nittler L. R., Alexander C. M. O'D., Gao X., Walker R. M. and Zinner E. (1997) Stellar sapphires: the properties and origins of presolar Al2O3 in meteorites. *Astrophys. J.* **483**, 475–495.

Nittler L. R., Alexander C. M. O'D., Gallino R., Hoppe P., Nguyen A. N., Stadermann F. J. and Zinner E. K. (2008) Aluminum-, calcium- and titanium-rich oxide stardust in ordinary chondrite meteorites. *Astrophys. J.* **682**, 1450–1478.

Nollett K. M., Busso M. and Wasserburg G. J. (2003) Cool bottom processes on the thermally pulsing asymptotic giant branch and the isotopic composition of circumstellar dust grains. *Astrophys. J.* **582**, 1036–1058.

Nuth J. A., Hallenbeck S. L. and Rietmeijer F. J. M. (2000) Laboratory studies of silicate smokes: analog studies of circumstellar materials. *J. Geophys. Res.* **105**, 10387–10396.

Ong W. J., Floss C. and Gyngard F. (2012) Negative secondary ion measurements of 54Fe/56Fe and 57Fe/56Fe in presolar silicate grains from Acfer 094. *Lunar Planet. Sci. XLIII.* Lunar Planet. Inst., Houston. #1225 (abstr.).

Ouellette N., Desch S. J., Bizarro M., Boss A. P., Ciesla F. and Meyer B. (2009) Injection mechanisms of short-lived radionuclides and their homogenization. *Geochim. Cosmochim. Acta* **73**, 4946–4962.

Palme H. and Fegley B. (1990) High-temperature condensation of iron-rich olivine in the solar nebula. *Earth Planet. Sci. Lett.* **101**, 180–195.

Posch Th., Kerschbaum F., Mutschke H., Dorschner J. and Jager C. (2002) On the origin of the 19.5 μm feature: identifying circumstellar Mg-Fe-oxides. *Astron. Astrophys.* **393**, L7–L10.

Posch Th., Kerschbaum F., Fabian D., Mutschke H., Dorschner J., Tamanai A. and Henning Th. (2003) Infrared properties of solid titanium oxides: exploring potential primary dust condensates. *Astrophys. J. Suppl.* **149**, 437–445.

Rietmeijer F. J. M., Nuth J. A. and Karner J. M. (1999) Metastable eutectic condensation in a Mg-Fe-SiO-H2-O2 vapor: analogs to circumstellar dust. *Astrophys. J.* **527**, 395–404.

Rietmeijer F. J. M., Pun A. and Nuth J. A. (2009) Dust formation and evolution in a Ca-Fe-SiO-H2-O2 vapour phase condensation experiment and astronomical implications. *Mon. Not. R. Astron. Soc.* **396**, 402–408.

Rodgers S. D. and Charnley S. B. (2008) Nitrogen superfractionation in dense cloud cores. *Mon. Not. R. Astron. Soc.* **385**, L48–L52.

Sandford S. A., Bernstein M. P. and Dworkin J. P. (2001) Assessment of the interstellar proceses leading to deuterium enrichment in meteoritic organics. *Meteorit. Planet. Sci.* **36**, 1117–1133.

Scott E. R. D. and Jones R. H. (1990) Disentangling nebular and asteroidal features of CO3 carbonaceous chondrite meteorites. *Geochim. Cosmochim. Acta* **54**, 2485–2502.

Scott E. R. D. and Krot A. N. (2005) Thermal processing of silicate dust in the solar nebula: clues from primitive chondrite matrices. *Astrophys. J.* **623**, 571–578.

Sloan G. C., Levan P. D. and Little-Marenin I. R. (1996) Sources of the 13 micron feature associated with oxygen-rich circumstellar dust. *Astrophys. J.* **463**, 310–319.

Sloan G. C. and Price S. D. (1998) The infrared spectral classification of oxygen-rich dust shells. *Astrophys. J. Suppl.* **119**, 141–158.

Sloan G. C., Kraemer K. E., Goebel J. H. and Price S. D. (2003) Guilt by association: the 13 micron dust emission feature and its correlation to other gas and dust features. *Astrophys. J.* **594**, 483–495.

Speck A. K., Barlow M. J., Sylvester R. J. and Hofmeister A. M. (2000) Dust features in the 10-μm infrared spectra of oxygen-rich evolved stars. *Astron. Astrophys. Suppl.* **146**, 437–464.

Stadermann F. J., Floss C., Bose M. and Lea A. S. (2009) The use of Auger spectroscopy for the in situ elemental characterization of sub-micrometer presolar grains. *Meteorit. Planet. Sci.* **44**, 1033–1049.

Stroud R. M., Floss C. and Stadermann F. J. (2009) Structure, elemental composition and isotopic composition of presolar silicates in MET 00426. *Lunar Planet. Sci. XL.* Lunar Planet. Inst., Houston. #1063 (abstr.).

Terzieva R. and Herbst E. (2000) The possibility of nitrogen isotopic fractionation in interstellar clouds. *Mon. Not. R. Astron. Soc.* **317**, 563–568.

Tielens A. G. G. M. (1998) Interstellar depletions and the life cycle of interstellar dust. *Astrophys. J.* **499**, 267–272.

Tielens A. G. G. M., Waters L. B. F. M., Molster F. J. and Justtanont K. (1998) Circumstellar silicate mineralogy. *Astrophys. Space Sci.* **255**, 415–426.

Vollmer C., Hoppe P. and Brenker F. E. (2008) Si isotopic compositions of presolar silicate grains from red giant stars and supernovae. *Astrophys. J.* **684**, 611–617.

Vollmer C., Hoppe P., Stadermann F. J., Floss C. and Brenker F. E. (2009a) NanoSIMS analysis and Auger electron spectroscopy of silicate and oxide stardust from the carbonaceous chondrite Acfer 094. *Geochim. Cosmochim. Acta* **73**, 7127–7149.

Vollmer C., Brenker F. E., Hoppe P. and Stroud R. M. (2009b) Direct laboratory analysis of silicate stardust from red giant stars. *Astrophys. J.* **700**, 774–782.

Vollmer C. and Hoppe P. (2010) First Fe isotopic measurement of a highly 17O-enriched stardust. *Lunar Planet. Sci. XLI.* Lunar Planet. Inst., Houston. #1200 (abstr.).

Wasserburg G. J., Boothroyd A. I. and Sackmann I. J. (1995) Deep circulation in red giant stars: a solution to the carbon and oxygen isotope puzzles? *Astrophys. J.* **447**, L37–L40.

Yada T., Floss C., Stadermann F. J., Zinner E., Nakamura T., Noguchi T. and Lea A. S. (2008) Stardust in Antarctic micrometeorites. *Meteorit. Planet. Sci.* **43**, 1287–1298.

Zega T. J., Nittler L. R., Busemann H., Hoppe P. and Stroud R. M. (2007) Coordinated isotopic and mineralogic analyses of planetary materials enabled by in situ lift-out with a focused ion beam scanning electron microscope. *Meteorit. Planet. Sci.* **42**, 1373–1386.

Zega T. J., Alexander C. M. O'D., Busemann H., Nittler L. R., Hoppe P., Stroud R. M. and Young A. F. (2010) Mineral associations and character of isotopically anomalous organic

material in the Tagish Lake carbonaceous chondrite. *Geochim. Cosmochim. Acta* **74**, 5966–5984.

Zega T. J., Alexander C. M. O'D., Nittler L. R. and Stroud R. M. (2011) A transmission electron microscopy study of presolar hibonite. *Astrophys. J.* **730**, 83–93.

Zinner E. (2007) Presolar grains. In *Treatise on Geochemistry Update 1* (eds. H. D. Holland and K. K. Turekian; vol. ed. A. M. Davis). Elsevier Ltd., Oxford, Online update only. pp. 1–33.

Associate editor: Trevor Ireland